



# **UNIVERSIDAD DE INVESTIGACIÓN DE TECNOLOGÍA EXPERIMENTAL YACHAY**

**Escuela de Ciencias Físicas y Nanotecnología**

**TÍTULO: Computational studies of the size-effect and temperature on  
the electronic structure and stability of TiO<sub>2</sub> nanoclusters**

Trabajo de integración curricular presentado como requisito para la  
obtención del título de Físico

**Autor:**

Sánchez Naranjo Jennifer Anaís

**Tutor:**

Pinto Esparza Henry Paúl, PhD.

**Co-Tutor:**

Alicja Mikołajczyk, PhD.

Urcuquí, octubre de 2021

**SECRETARÍA GENERAL**  
**(Vicerrectorado Académico/Cancillería)**  
**ESCUELA DE CIENCIAS FÍSICAS Y NANOTECNOLOGÍA**  
**CARRERA DE FÍSICA**  
**ACTA DE DEFENSA No. UITEY-PHY-2021-00025-AD**

A los 21 días del mes de diciembre de 2021, a las 12:00 horas, de manera virtual mediante videoconferencia, y ante el Tribunal Calificador, integrado por los docentes:

<b>Presidente Tribunal de Defensa</b>	Dr. VACACELA GOMEZ, CRISTIAN ISAAC , Ph.D.
<b>Miembro No Tutor</b>	Dr. CHIMBORAZO GUERRON, JOHNNY FABRICIO , Ph.D.
<b>Tutor</b>	Dr. PINTO ESPARZA, HENRY PAUL , Ph.D.

El(la) señor(ita) estudiante **SANCHEZ NARANJO, JENNIFER ANAIS**, con cédula de identidad No. **1804794434**, de la **ESCUELA DE CIENCIAS FÍSICAS Y NANOTECNOLOGÍA**, de la Carrera de **FÍSICA**, aprobada por el Consejo de Educación Superior (CES), mediante Resolución **RPC-SO-39-No.456-2014**, realiza a través de videoconferencia, la sustentación de su trabajo de titulación denominado: **Computational studies of the size-effect and temperature on the electronic structure and stability of TiO2 nanoclusters.** , previa a la obtención del título de **FÍSICO/A**.

El citado trabajo de titulación, fue debidamente aprobado por el(los) docente(s):

<b>Tutor</b>	Dr. PINTO ESPARZA, HENRY PAUL , Ph.D.
--------------	---------------------------------------

Y recibió las observaciones de los otros miembros del Tribunal Calificador, las mismas que han sido incorporadas por el(la) estudiante.

Previamente cumplidos los requisitos legales y reglamentarios, el trabajo de titulación fue sustentado por el(la) estudiante y examinado por los miembros del Tribunal Calificador. Escuchada la sustentación del trabajo de titulación a través de videoconferencia, que integró la exposición de el(la) estudiante sobre el contenido de la misma y las preguntas formuladas por los miembros del Tribunal, se califica la sustentación del trabajo de titulación con las siguientes calificaciones:

Tipo	Docente	Calificación
Miembro Tribunal De Defensa	Dr. CHIMBORAZO GUERRON, JOHNNY FABRICIO , Ph.D.	9,5
Presidente Tribunal De Defensa	Dr. VACACELA GOMEZ, CRISTIAN ISAAC , Ph.D.	10,0
Tutor	Dr. PINTO ESPARZA, HENRY PAUL , Ph.D.	10,0

Lo que da un promedio de: **9.8 (Nueve punto Ocho)**, sobre 10 (diez), equivalente a: **APROBADO**

Para constancia de lo actuado, firman los miembros del Tribunal Calificador, el/la estudiante y el/la secretario ad-hoc.

*Certifico que en cumplimiento del Decreto Ejecutivo 1017 de 16 de marzo de 2020, la defensa de trabajo de titulación (o examen de grado modalidad teórico práctica) se realizó vía virtual, por lo que las firmas de los miembros del Tribunal de Defensa de Grado, constan en forma digital.*

SANCHEZ NARANJO, JENNIFER ANAIS  
**Estudiante**

Dr. VACACELA GOMEZ, CRISTIAN ISAAC , Ph.D.  
**Presidente Tribunal de Defensa**

Dr. PINTO ESPARZA, HENRY PAUL , Ph.D.  
**Tutor**

**HENRY PAUL PINTO ESPARZA**  
 Digitally signed by  
 HENRY PAUL PINTO  
 ESPARZA  
 Date: 2021.12.21  
 14:02:49 -05'00'

Dr. CHIMBORAZO GUERRON, JOHNNY FABRICIO , Ph.D.  
**Miembro No Tutor**



Firmado electrónicamente por:  
**JOHNNY FABRICIO  
CHIMBORAZO  
GUERRON**

CIFUENTES TAFUR, EVELYN CAROLINA  
**Secretario Ad-hoc**

EVELYN  
CAROLINA  
CIFUENTES TAFUR

Firmado digitalmente por  
EVELYN CAROLINA  
CIFUENTES TAFUR  
Fecha: 2021.12.21 13:04:16  
-05'00'

## Autoría

Yo, **Jennifer Anaís Sánchez Naranjo**, con cédula de identidad **1804794434**, declaro que las ideas, juicios, valoraciones, interpretaciones, consultas bibliográficas, definiciones y conceptualizaciones expuestas en el presente trabajo, así como los procedimientos y herramientas utilizadas en la investigación, son de absoluta responsabilidad de la autora del trabajo de integración curricular. Así mismo, me acojo a los reglamentos internos de la Universidad de Investigación de Tecnología Experimental Yachay.

Urcuquí, octubre 2021.



Jennifer Anaís Sánchez Naranjo  
C.I. 1804794434

## **Autorización de publicación**

Yo, **Jennifer Anaís Sánchez Naranjo**, con cédula de identidad **1804794434**, cedo a la Universidad de Tecnología Experimental Yachay, los derechos de publicación de la presente obra, sin que deba haber un reconocimiento económico por este concepto. Declaro además que el texto del presente trabajo de titulación no podrá ser cedido a ninguna empresa editorial para su publicación u otros fines, sin contar previamente con la autorización escrita de la Universidad.

Asimismo, autorizo a la Universidad para que realice la digitalización y publicación de este trabajo de integración curricular en el repositorio virtual, de conformidad a lo dispuesto en el Art. 144 de la Ley Orgánica de Educación Superior.

Urcuquí, octubre 2021.



Jennifer Anaís Sanchez Nájranjo  
C.I. 1804794434

## Acknowledgements

First of all, I want to deeply thank Dr. Henry Pinto, for being my guide, tutor and friend throughout this journey. None of this would have been possible without all his support, guidance and constant motivation that was present from the very beginning of the career until the end of it. Being able to join and develop research in CompNano group has been one of the most enriching and rewarding experiences of my entire academic life. Additionally, this project would not have been possible without my co-tutor Dr. Alicja Mikołajczyk, a deep appreciation for all her contributions.

I want to express my most sincere thanks to my parents Germania Naranjo and Fabian Sánchez, who have given me all their support, understanding and love from the very first day I came into their lives. Thanks for always believing in me even when I didn't myself. The person that I have become today is thanks to them, who have taught me the most important lessons in life: kindness, love and hard work. I hope a little part of all their efforts is reflected in this academic achievement. I also want to thank my brother Christian, that taught me the importance of standing for myself and the people I love, to navigate through this life in the best way possible with the head always held high. Miriam Pico, I want to thank you for always taking care of me and being my actual family.

I want to sincerely thank my friends, the family that I heartily chose: Dayanara Yáñez, for being there for me since high school, Jonathan Freire, for being always true, Johana Telenchana, for being my first friend in Yachay, Carito Ibarra, for being my voice of the reason, Mateo Narváez, for being my dear friend through all the career and Camila Velasteguí, for absolutely everything that connect us both. Raúl Hidalgo, thank you for standing by my side, and believing in me.

I keep you all forever in my heart.

## Resumen

El óxido de titanio, con tres fases cristalinas diferentes, es uno de los óxidos metálicos de transición más importante debido a sus propiedades fotocatalíticas, electrónicas e incluso biológicas<sup>1,2</sup>. Sin embargo, el rendimiento de los nanoclusters de TiO<sub>2</sub> depende fuertemente de su tamaño, forma y organización. Aunque los estudios teóricos de los nanoclusters de TiO<sub>2</sub> se han realizado en gran medida<sup>3,4</sup>, aún se necesitan resolver algunos desafíos para utilizar sus propiedades de la manera más práctica. Una combinación del método semi-empírico de densidad funcional tight-binding (DFTB) con la teoría funcional de la densidad *ab initio* (DFT) nos permitirán predecir y estudiar nanoclusters de TiO<sub>2</sub>, de manera que podamos predecir el nanocluster con la topología más estable dadas dos restricciones: el número de moléculas de TiO<sub>2</sub> y la temperatura. Se aplican simulaciones de dinámica molecular para resolver la estructura atómica más probable de los nanoclusters n(TiO<sub>2</sub>) (n = 1–10) a temperatura ambiente. La estructura electrónica de los candidatos más probables es calculada utilizando ab-initio DFT a nivel de el funcional híbrido B3LYP. Propiedades fisico-químicas como la energía electrónica, repulsión nuclear, momento dipolar, momento cuadrupolo, polarizabilidad, HOMO, LUMO, becha de energy, energía de punto cero y radio de giro también son predecidas.

**Keywords:** Teoría de densidad-funcional, método semi-empírico tight binding, nanoclusters, estructura electrónica, dinámica molecular, efecto del tamaño.



## Abstract

Titanium oxide with three different crystalline phases is an important transition metal oxide due to its photocatalytic, electronic, and even biological properties<sup>1,2</sup>. However, the performance of the TiO<sub>2</sub> nanoclusters strongly depends on their size, shape, organization. Even though theoretical studies of TiO<sub>2</sub> nanoclusters have been largely performed<sup>3,4</sup>, some challenges are still needed to solve in order to utilize its properties in the most practical way. A combination of semi-empirical density-functional tight-binding (DFTB) with ab initio density-functional theory (DFT) methods will allow us to predict and study TiO<sub>2</sub> nanoclusters, such that we can resolve the most stable nanocluster topology given two constraints: the number of TiO<sub>2</sub> molecules and the temperature T. Molecular dynamics simulations are applied to resolve the most likely atomic structure of n(TiO<sub>2</sub>) (n = 1–10) nanoclusters at a room temperature. The electronic structure of the most likely candidates are computed using ab-initio DFT at the level of hybrid functional B3LYP. Physical-chemical properties like electronic energy, nuclear repulsion, dipole moment, quadrupole moment, polarizability, HOMO, LUMO, band gap, zero-point energy and gyration radius are also predicted.

**Keywords:** Density-functional theory, semi-empirical tight binding method, nanoclusters, electronic-structure, molecular dynamics, size effect.



# Contents

<b>List of Figures</b>	<b>xii</b>
<b>List of Tables</b>	<b>xiv</b>
<b>List of Papers</b>	<b>xv</b>
<b>1 Introduction</b>	<b>1</b>
1.1 Problem Statement . . . . .	2
1.2 General and Specific Objectives . . . . .	3
<b>2 Theoretical Background</b>	<b>5</b>
2.1 Many-body system Schrödinger equation . . . . .	5
2.1.1 Atomic units . . . . .	7
2.2 Solid state physics approximations . . . . .	9
2.2.1 The Born-Oppenheimer (BO) approximation . . . . .	9
2.2.2 Independent electron approximation . . . . .	10
2.2.3 Hartree-Fock (HF) theory . . . . .	11
2.3 Density Functional Theory (DFT) principles . . . . .	14
2.3.1 Hohenberg-Kohn Theorem . . . . .	14
2.3.2 Kohn-Sham theory . . . . .	15
2.3.3 Self-consistent calculations . . . . .	17
2.4 Exchange-correlation functional $E_{xc}$ . . . . .	18
2.4.1 The local spin density approximation (LSDA) . . . . .	18
2.4.2 The generalized gradient approximation (GGA) . . . . .	20

2.4.3	The meta-GGA . . . . .	20
2.4.4	Hybrid functionals . . . . .	21
2.5	Basis set . . . . .	22
2.5.1	Gaussian-Type orbitals . . . . .	23
2.6	RIJCOSX Algorithm . . . . .	23
2.7	Tight Binding (TB) . . . . .	24
2.8	Molecular Dynamics (MD) theory . . . . .	24
2.8.1	Verlet algorithm . . . . .	25
<b>3</b>	<b>Methodology</b>	<b>27</b>
3.1	Computational modelling methods . . . . .	27
3.1.1	Extended tight-binding ( <i>xTB</i> ) package . . . . .	27
3.1.2	ORCA . . . . .	28
3.2	Computational procedure for cluster development . . . . .	28
3.2.1	Construction of the clusters in ASE . . . . .	29
3.2.2	<i>xTB</i> pre-relaxation and Molecular Dynamics (MD). . . . .	30
3.2.3	ORCA relaxation . . . . .	35
<b>4</b>	<b>Results &amp; Discussion</b>	<b>37</b>
4.1	Molecular dynamics simulations and electronic structure of $(\text{TiO}_2)_n$ , $n = 1 - 10$ clusters and electronic distribution calculations. . . . .	37
4.2	Predicted physical properties of the clusters and correlations. . . . .	53
4.3	Stability of the clusters: Magic clusters. . . . .	58
<b>5</b>	<b>Conclusions &amp; Outlook</b>	<b>61</b>
<b>6</b>	<b>Appendix</b>	<b>63</b>
6.1	Size-Dependence of physical properties in clusters. . . . .	63
	<b>Bibliography</b>	<b>69</b>

# List of Figures

2.1	Density functional theory exchange-correlation functional approximations hierarchy according to Jacob's ladder. . . . .	19
3.1	Extended tight binding GFNn-xTB logo <sup>5</sup> . . . . .	28
3.2	ORCA logo <sup>6</sup> . . . . .	28
3.3	Schematic diagram of the process to obtain the electronic structure and other physical properties from $(TiO_2)_n$ (n = 1-10) nanoclusters . . . . .	29
3.4	6f2.xyz GFNn-xTB input file. . . . .	31
3.5	Command line for opening ASE. . . . .	31
3.6	Command line for pre-relaxation performed in xTB with 4 cores. . . . .	32
3.7	A production input file used in GFN2-xTB to compute the molecular dynamics in $TiO_2$ nanoclusters. . . . .	32
3.8	Molecular dynamics (MD) at room temperature ( T = 298.15 K) for 1 ns of 6f2 $TiO_2$ nanocluster. . . . .	33
3.9	Molecular dynamics of 4c2 nanocluster at room temperature (T = 298.15 K) for 0.5 ns , where each of the MD graphs correspond to an specific $\Delta t$ . <b>A</b> : 1 fs; <b>B</b> : 2 fs; <b>C</b> : 3 fs; <b>D</b> : 4 fs; <b>E</b> : 5 fs; <b>F</b> : 7 fs. . . . .	34
3.10	A production input file used in ORCA to compute the relaxation and electronic properties of the cluster. . . . .	35
4.1	Molecular dynamics of $(TiO_2)_2$ nanoclusters. <b>A</b> : 2a1; <b>B</b> : 2a2; <b>C</b> : 2a3. . . . .	38
4.2	Molecular dynamics of $(TiO_2)_3$ nanoclusters. <b>A</b> : 3b1; <b>B</b> : 3b2; <b>C</b> : 3b3; <b>D</b> : 3b4. . . . .	39
4.3	Molecular dynamics of $(TiO_2)_4$ nanoclusters. <b>A</b> : 4c1; <b>B</b> : 4c2; <b>C</b> : 4c3; <b>D</b> : 4c4. . . . .	40
4.4	Molecular dynamics of $(TiO_2)_5$ nanoclusters. <b>A</b> : 5d1; <b>B</b> : 5d2; <b>C</b> : 5d3. . . . .	41

4.5	Molecular dynamics of $(TiO_2)_6$ nanoclusters. <b>A</b> : 6f1; <b>B</b> : 6f2. . . . .	42
4.6	Molecular dynamics of $(TiO_2)_7$ nanoclusters. <b>A</b> : 7g1; <b>B</b> : 7g2; <b>C</b> : 7g3. . . . .	43
4.7	Molecular dynamics of $(TiO_2)_8$ nanoclusters. <b>A</b> : 8h2; <b>B</b> : 8h3; <b>C</b> : 8h4. . . . .	44
4.8	Molecular dynamics of $(TiO_2)_9$ nanoclusters. <b>A</b> : 9i1; <b>B</b> : 9i2. . . . .	45
4.9	Molecular dynamics of $(TiO_2)_{10}$ nanoclusters. <b>A</b> : 10j1; <b>B</b> : 10j2; <b>C</b> : 10j3. . . . .	46
4.10	Summary of all possible configurations of nanoclusters. . . . .	54
4.11	Correlation matrix of the different physical-chemical properties predicted by B3LYP electronic structure calculations. . . . .	57
4.12	Energy stability ( $\Delta^2 E$ ) with respect to the number of $(TiO_2)_n$ molecules. . . . .	59
6.1	Size-dependence of the total energy ( $E_{tot}$ ) of the clusters with the gyration ratio ( $R_g$ ). . . . .	63
6.2	Size-dependence of the electronic energy ( $E_{elec}$ ) of the clusters with the gyration ratio ( $R_g$ ). . . . .	64
6.3	Size-dependence of the isotropic polarizability ( $P$ ) of the clusters with the gyra- tion ratio ( $R_g$ ). . . . .	65
6.4	Size-dependence of the nuclear repulsion ( $E_{NR}$ ) of the clusters with the gyration ratio ( $R_g$ ). . . . .	66
6.5	Size-dependence of the quadrupole moment ( $Q$ ) of the clusters with the gyration ratio ( $R_g$ ). . . . .	67
6.6	Size-dependence of the zero-point energy ( $E_{ZP}$ ) of the clusters with the gyration ratio ( $R_g$ ). . . . .	68

# List of Tables

4.1	Result summary: Original vs. most-stable relaxed structure plus HOMO distribution. . . . .	47
4.2	DFT-B3LYP computed results: total Energy ( $E_{tot}$ ), dipole moment ( $p$ ), quadrupole moment ( $Q$ ), isotropic polarizability ( $P$ ), electronic Energy ( $E_{elec}$ ), nuclear repulsion ( $E_{NR}$ ), HOMO, LUMO, energy gap ( $E_g$ ), zero-point energy ( $E_{ZP}$ ) and Gyration radius ( $R_g$ ). In this table, $p$ , $Q$ and $\alpha$ is given in a.u., the energies in Ha and $R_g$ in Å. . . . .	55



# Chapter 1

## Introduction

Nanomaterials modeling has become one of the fastest-growing fields within the materials sciences and solid-state physics in general, allowing the scientific community to make considerable advances in the study of nanomaterials manipulations. This field of research makes possible the creation of novel properties such as fluorescence, extreme anisotropy of electrical and mechanical properties, high electron mobility, tunable band-gap, which in the past were not possible to study<sup>7</sup>.

From the economics and social point of view, the impact of materials modeling has been gaining importance through the years, resulting in materials and products that are manufactured industrially and have the potential to become an improvement at many scales<sup>8</sup>. At a macro scale, the novel properties found out through materials modeling are able to have an impact on environmental emissions, waste production, natural resource depletion, innovation, economic development, quality of life, etc<sup>9</sup>. At the nanoscale, it has catalyzed the enhancement of science and technology, resulting in miniaturization, high computer performance chips, nano-based drug delivery systems, etc<sup>7</sup>.

Density Functional Theory (DFT) has become one the most widely used tool in the field of materials modeling, becoming quickly the most heavily cited concept in the physical sciences, making part of the most cited papers in history, including two papers in the top10<sup>10</sup>. The fundamental idea of DFT states that any atomic system formed by electrons and nuclei can be described with enough accuracy within a certain tolerance by using only the total charge density. This supposes a huge improvement since in the past it was thought that many-electron wave

function that scientists were essential to complete any atomic description<sup>11</sup>. DFT applications are very extensive, enabling to study chemistry, biochemistry, biology, nanosystems, and materials<sup>10</sup>. In other words, DFT became one of the major breakthroughs for studying atoms, molecules, gases, liquids, and solids. This work will concentrate on one particular atomic structure: Titanium dioxide ( $TiO_2$ ) nanoclusters.

Nanostructured titanium dioxide has significant importance in the industry and scientific fields due to its variety of properties and applications, such as energy conversion<sup>12</sup>, photocatalytic degradation of pollutants<sup>1</sup>, sensor electronics for detection of gases, biological material, or chemicals<sup>2</sup>, in drug delivery<sup>13,14</sup>, etc. In general, the physical and chemical properties of  $TiO_2$  are conditioned by the specific electronic structure of each cluster depending on its size, shape, organization, etc<sup>14</sup>. Subsequently, figuring out the structure-property correlations is essential in order to utilize its properties in the most practical way<sup>14</sup>. Even though theoretical studies of  $TiO_2$  nanoclusters have been largely performed<sup>3,4</sup>, some challenges are still needed to solve, such as the optimal cluster size to tackle some particular problems<sup>14</sup>. DFT calculations allow us to perform extensive studies on nanostructured material such as clusters, which otherwise would be impossible due to their scale<sup>14-17</sup>. In this sense, our goal is to study the electronic structure properties of  $TiO_2$  nanoclusters employing state-of-the-art density functional theory methods.

## 1.1 Problem Statement

In general, it is a known fact that the properties of nanoparticles are significantly different from fine particles or bulk materials; then, it is not possible to extrapolate any results from those types of studies. Moreover, most of the key physicochemical properties of nanoparticles can be easily altered by changing the size of the structure. Then, it is essential to have a precise size-sensitive property sense to exploit the various advantages and technological applications of nanoclusters. However, there is currently a lack of consistent and detailed databases from where we find a description for the size effect in the physicochemical properties of nanoparticles. Nevertheless, carrying on with a study to obtain systematic data that reflect the change of the properties and the size requires very time-consuming procedures and is experimentally costly. Furthermore, the size effect in the nanoparticle properties makes it difficult to study with the existing traditional methodology. Then, this problem presents many favorable challenges that can be sorted with the

appropriate implementations of different procedures.

## 1.2 General and Specific Objectives

The main objective of this thesis is to compute with a semi-empirical density-functional tight binding (DFTB) and *ab initio* density-functional theory the electronic structure of TiO<sub>2</sub> nanoclusters. Specifically, we aim to:

- Explain the theoretical foundations of DFT with a focus on the B3LYP hybrid functional.
- Explain the methodology for studying TiO<sub>2</sub> nanoclusters.
- Study the all the possible meta-stable configurations of TiO<sub>2</sub> nanoclusters performing molecular dynamics simulations at 298.15 K.
- Study the stability of all the possible meta-stable configurations of TiO<sub>2</sub> through an all-electron *ab initio* DFT full relaxation.
- Find trends and likely correlations between the size of the nanoclusters and physical-chemical properties such as: total Energy ( $E_{tot}$ ), dipole moment ( $p$ ), quadrupole moment ( $Q$ ), isotropic polarizability ( $P$ ), electronic Energy ( $E_{elec}$ ), nuclear repulsion ( $E_{NR}$ ), HOMO, LUMO, energy gap ( $E_g$ ), zero-point energy ( $ZPE$ ).



# Chapter 2

## Theoretical Background

### 2.1 Many-body system Schrödinger equation

As a first step to understand the different material properties of our system in a non-relativistic we need to keep in mind that, at the atomic scale, they are just collections of electrons and nuclei disposed in a characteristic electronic structure; such that this disposition gives us all the physical properties of the solids<sup>18</sup>.

Then, in order to study the behavior of quantum particles we consider the many-body Schrödinger equation:

$$\hat{H}\Psi = [\hat{T} + \hat{V}]\Psi = \hat{E}_{tot}\Psi, \quad (2.1)$$

Where  $\hat{H}$  represents the Hamiltonian of the system, that contains the information of the kinetic energy ( $\hat{T}$ ) and potential energy ( $\hat{V}$ ) operators, respectively.  $\hat{E}_{tot}$  is the total energy operator, and  $\Psi$  is so called many-body wavefunction. Considering a  $M$  nuclei system with coordinates  $\mathbf{R}_1, \mathbf{R}_2, \dots, \mathbf{R}_M$  and  $N$  electrons with coordinates  $\mathbf{r}_1, \mathbf{r}_2, \dots, \mathbf{r}_N$ , we obtain a wavefunction with shape:

$$\Psi = \Psi(\mathbf{r}_1, \mathbf{r}_2, \dots, \mathbf{r}_N; \mathbf{R}_1, \mathbf{R}_2, \dots, \mathbf{R}_M). \quad (2.2)$$

Following the same notation, the kinetic energy operator ( $\hat{K}$ ) can be described as:

$$K = - \sum_{i=1}^N \frac{\hbar^2}{2m_e} \nabla_i^2 - \sum_{I=1}^M \frac{\hbar^2}{2M_I} \nabla_I^2, \quad (2.3)$$

Where  $M_I$  are the masses of the nuclei,  $m_e$  is the mass of the electron,  $\hbar$  is the reduced Planck's constant and  $\nabla_i^2$  and  $\nabla_I^2$  are the Laplacian operators acting on the electrons and nuclei respective coordinates.

For the potential energy operator ( $\hat{V}$ ) we need to take in count three Coulombic interactions: electron-electron  $\hat{V}_{e-e}$ , nuclei-nuclei  $\hat{V}_{n-n}$  and nuclei-electron  $\hat{V}_{n-e}$ :

$$\hat{V} = \hat{V}_{e-e} + \hat{V}_{n-n} + \hat{V}_{n-e}, \quad (2.4)$$

First, we have the  $\hat{V}_{e-e}$  Coulombic repulsion, due to the negative charge of the electrons, which is described as:

$$V_{e-e} = \frac{1}{2} \sum_{i \neq j} \frac{e^2}{4\pi\epsilon_0} \frac{1}{|\mathbf{r}_i - \mathbf{r}_j|}, \quad (2.5)$$

Where  $e$  is the charge of the electron and  $\epsilon_0$  is the permeability in free space. The indices  $i$  and  $j$  are defined in the range  $[1, N]$ , and are always different since an electron will never repel to itself. The  $\frac{1}{2}$  is introduced in order to count just one energy contribution per electron pair.  $V_{e-e}$  is positive due to its repulsive nature.

Second, we have the  $\hat{V}_{n-n}$  Coulombic repulsion that is described as:

$$V_{n-n} = \frac{1}{2} \sum_{I \neq J} \frac{e^2}{4\pi\epsilon_0} \frac{Z_I Z_J}{|\mathbf{R}_I - \mathbf{R}_J|}, \quad (2.6)$$

Where  $Z_{I(J)}$  represent the atomic numbers of each nuclei  $I(J)$ . The index logic and contributions of equation (2.5) applies for (2.6) too.

Third, we have the  $\hat{V}_{e-n}$  Coulombic attraction, due to the opposite charge nature of the electron and nuclei, described as:

$$V_{e-n} = - \sum_{i \neq I} \frac{e^2}{4\pi\epsilon_0} \frac{Z_I}{|\mathbf{r}_i - \mathbf{R}_I|}, \quad (2.7)$$

The same index logic in equations (2.5) and (2.6) applies for (2.7). This contribution is positive due to its attractive nature.

Finally, substituting equations (2.3),(2.4),(2.5), (2.6) and (2.7) definitions in (2.1) we can write the many-body Schrödinger equation as:

$$\left[ - \sum_{i=1}^N \frac{\hbar^2}{2m_e} \nabla_i^2 - \sum_{I=1}^M \frac{\hbar^2}{2M_I} \nabla_I^2 + \frac{e^2}{4\pi\epsilon_0} \left( \frac{1}{2} \sum_{i \neq j} \frac{1}{|\mathbf{r}_i - \mathbf{r}_j|} + \frac{1}{2} \sum_{I \neq J} \frac{Z_I Z_J}{|\mathbf{R}_I - \mathbf{R}_J|} - \sum_{i \neq I} \frac{Z_I}{|\mathbf{r}_i - \mathbf{R}_I|} \right) \right] \Psi = E_{tot} \Psi. \quad (2.8)$$

At this point, it is worth mentioning that the wavefunction for a specific set of coordinates (2.2) cannot be measured in experiments, due to it is not a physical observable. For instance, the quantity that is physically interesting is, in fact, the probability of simultaneously finding  $N$  electrons in  $\mathbf{r}_i$  positions<sup>19</sup>, that is described as:

$$|\Psi|^2 = |\Psi(\mathbf{r}_1, \dots, \mathbf{r}_N; \mathbf{R}_1, \dots, \mathbf{R}_M)|^2. \quad (2.9)$$

Then, the probability of finding any electron (indifferently of the  $i$  label) at position  $\mathbf{r}$  is<sup>18</sup>:

$$n(\mathbf{r}) = N \int |\Psi|^2 d\mathbf{r}_2 \dots d\mathbf{r}_N d\mathbf{R}_1 \dots d\mathbf{R}_M. \quad (2.10)$$

Normalizing the wavefunction (2.2) to 1, we obtain:

$$\int |\Psi|^2 d\mathbf{r}_2 \dots d\mathbf{r}_N d\mathbf{R}_1 \dots d\mathbf{R}_M = 1. \quad (2.11)$$

Introducing the condition of equation (2.11) in (2.10), as you may have expected, we obtain that integrating the electronic charge density through all the volume results in the total number of electrons.

$$\int n(\mathbf{r}) d\mathbf{r} = N. \quad (2.12)$$

Additionally, it is essential to mention that the solution of equation (2.8) for every system bigger than the He atom remains practically impossible for analytic approaches, and numerical solutions are too computationally expensive. This is due to the complexity of the solutions escalating exponentially with the number of atoms in the system<sup>18,19</sup>.

### 2.1.1 Atomic units

Some simplifications can be applied to equation 2.8 using the atomic units to facilitate calculations. First, we observe in (2.8) does not depend on any empirical parameter, therefore this is a ‘first-principles approach’ for the study of material properties<sup>18</sup>. In contrast, the fundamental physical

constants that intervene in these calculations are:

$$\begin{aligned}
\hbar &= 1.05457163 \cdot 10^{-34} J \cdot s, \\
m_e &= 9.10938291 \cdot 10^{-31} kg, \\
m_p &= 1.67262164 \cdot 10^{-27} kg, \\
e &= 1.60217649 \cdot 10^{-19} C, \\
\epsilon_0 &= 8.85418782 \cdot 10^{-12} F/m.
\end{aligned} \tag{2.13}$$

Additionally, let's consider the Born radius  $a_0 = 0.529 \text{ \AA}$ , which is the average radius of electron orbital for hydrogen atom in its fundamental state.

Using the approach presented in ref.<sup>18</sup>, we can define the average Coulomb energy for an electron–proton pair in terms of the previous fundamental constants (for more detailed derivation, see ref.<sup>18</sup>):

$$E_{Ha} = \frac{e^2}{4\pi\epsilon_0 a_0} = \frac{\hbar^2}{m_e a_0^2}. \tag{2.14}$$

Where, 'Ha' stands for 'Hartree'. Moreover, it is obtained that kinetic energy for the Hydrogen model is of the order of Hartree energy ( $E_{Ha}$ ), making it a natural unit of energy for many-body Schrödinger equation.

Then, we take equation 2.8 and divide it by  $E_{Ha}$ . obtaining:

$$\left( - \sum_{i=1}^N \frac{1}{2} a_0^2 \nabla_i^2 - \sum_{I=1}^M \frac{1}{2} \frac{a_0^2}{M_I/m_e} \nabla_I^2 + \frac{1}{2} \sum_{i \neq j} a_0 \frac{1}{|\mathbf{r}_i - \mathbf{r}_j|} + \frac{1}{2} \sum_{I \neq J} a_0 \frac{Z_I Z_J}{|\mathbf{R}_I - \mathbf{R}_J|} - \sum_{i \neq I} a_0 \frac{Z_I}{|\mathbf{r}_i - \mathbf{R}_I|} \right) \Psi = \frac{E_{tot}}{E_{Ha}} \Psi. \tag{2.15}$$

From here we will consider the following units to define energy, distances and masses, respectively:

$$\begin{aligned}
1Ha &= 27.2114 eV = 4.3597 \cdot 10^{18} J, \\
1bohr &= 0.529177 \text{ \AA} = 0.529177 \cdot 10^{10} m, \\
1a.u. &= 9.10938291 \cdot 10^{31} kg.
\end{aligned} \tag{2.16}$$

Additionally, we will set electron charge  $e = 1$ . These set of units are the so-called Hartree atomic units that will be used from now on. Rewriting equation 2.8 in terms of the Hartree unit we get the following simplified form:

$$\left( - \sum_{i=1}^N \frac{1}{2} \nabla_i^2 - \sum_{I=1}^M \frac{1}{2} \frac{\nabla_I^2}{M_I} + \frac{1}{2} \sum_{i \neq j} \frac{1}{|\mathbf{r}_i - \mathbf{r}_j|} + \frac{1}{2} \sum_{I \neq J} \frac{Z_I Z_J}{|\mathbf{R}_I - \mathbf{R}_J|} - \sum_{i \neq I} \frac{Z_I}{|\mathbf{r}_i - \mathbf{R}_I|} \right) \Psi = E_{tot} \Psi, \tag{2.17}$$

This form of the many-body Schrodinger equation is the most common in material modelling from first-principles since the only parameter introduced are the atomic masses  $M_I$  and the atomic masses  $M_{I,J}$ .

## 2.2 Solid state physics approximations

### 2.2.1 The Born-Oppenheimer (BO) approximation

Born-Oppenheimer approximation states that the many-body total wavefunction can be expressed as the product of independent functions: the nuclear wavefunction  $\chi$  (depending only on nuclear coordinates keeping the electrons in some fixed state) and the electronic wavefunction  $\Psi_{\mathbf{R}}$  (depending only on electronic coordinates keeping the nuclei at fixed positions)<sup>20</sup>, as:

$$\Psi(\mathbf{r}_1, \dots, \mathbf{r}_N; \mathbf{R}_1, \dots, \mathbf{R}_M) \approx \underbrace{\chi(\mathbf{R}_1, \dots, \mathbf{R}_M)}_{\text{nuclei}} \times \underbrace{\Psi_{\mathbf{R}}(\mathbf{r}_1, \dots, \mathbf{r}_N)}_{\text{electrons}}. \quad (2.18)$$

Additionally, in this approximation is implied that the electrons contribute with potential energy to the motion of the nuclei, while the moving nuclei deform the wavefunction of the electron continuously, with no abrupt changes. Hence, BO approximation is also called adiabatic approximation<sup>20</sup>.

In general, atoms' masses are about  $10^4$ - $10^5$  larger than electrons' masses, consequently, the electrons will be  $10^2$ - $10^3$  faster than the nuclei at the same kinetic energy. Then, it is reasonable to assume that electrons follow the motion of the nuclei almost instantaneously. Therefore, setting  $M_I \approx \infty$ , the nuclei kinetic energy term in equation (2.17) becomes negligible.

$$\sum_{I=1}^M \frac{1}{2} \frac{\nabla_I^2}{M_I} \approx 0. \quad (2.19)$$

Let us also consider the following definitions for the energy of system and the Coulomb potential of the nuclei experienced by the electrons<sup>18</sup>:

$$E = E_{tot} - \frac{1}{2} \sum_{I \neq J} \frac{Z_I Z_J}{|\mathbf{R}_I - \mathbf{R}_J|}, \quad (2.20)$$

and,

$$V_n(\mathbf{r}) = - \sum_I \frac{Z_I}{|\mathbf{r} - \mathbf{R}_I|}. \quad (2.21)$$

For convenience, from now on the nuclear coordinates  $R_l$  are regarded as external parameters, such that  $\Psi$  depends only on the electron coordinates. Taken together these definitions we can replace then in equation (2.17) to rewrite is in a much more simple manner:

$$\left( -\sum_{i=1}^N \frac{1}{2} \nabla_i^2 + \sum_i V_n(\mathbf{r}_i) + \frac{1}{2} \sum_{i \neq j} \frac{1}{|\mathbf{r}_i - \mathbf{r}_j|} \right) \Psi = E\Psi, \quad (2.22)$$

### 2.2.2 Independent electron approximation

In order to study the electronic structure through equation (2.22) we will eliminate the electronic Coulomb repulsion term, such that, electrons would not sense each other<sup>18</sup>.

First, let us define the many electron Hamiltonian as:

$$\hat{H}(\mathbf{r}_1, \dots, \mathbf{r}_N) = -\sum_{i=1}^N \frac{1}{2} \nabla_i^2 + \sum_i V_n(\mathbf{r}_i; \mathbf{R}) + \frac{1}{2} \sum_{i \neq j} \frac{1}{|\mathbf{r}_i - \mathbf{r}_j|}. \quad (2.23)$$

Transforming equation (2.22) in simply:

$$\hat{H}\Psi = E\Psi. \quad (2.24)$$

Looking at equation (2.23) results natural to define a single electron Hamiltonian:

$$\hat{H}_0(\mathbf{r}) = -\frac{1}{2} \nabla^2 + V_n(\mathbf{r}). \quad (2.25)$$

Notice that in equation (2.25) electronic Coulomb integration is switched off since we are within the independent electron approximation. This dramatic simplification is necessary due to the significant complications it carries for the analytical solving. Following these definitions, Schrödinger equation within the independent electron approximation would become:

$$\sum_i \hat{H}_0(\mathbf{r}_i) \Psi = E\Psi, \quad (2.26)$$

For instance, since each electron is independent of the other, the probability of finding a particular electron  $i$  at position  $r_i$  will simply come from the product of the individual electronic probabilities  $|\phi_i(\mathbf{r}_i)|^2$ . Therefore,  $\Psi$  is redefined as:

$$\Psi(\mathbf{r}_1, \dots, \mathbf{r}_N) = \phi_1(\mathbf{r}_1) \dots \phi_N(\mathbf{r}_N), \quad (2.27)$$

For instance, each of the individual wave functions  $\phi_i(\mathbf{r}_i)$  can be solved using the single electron Hamiltonian (2.25). Hence, replacing definition (2.27) into equation (2.26) we get:

$$\sum_i [\hat{H}_0(\mathbf{r}_i)] \phi_1(\mathbf{r}_1) \dots \phi_N(\mathbf{r}_N) = E \phi_1(\mathbf{r}_1) \dots \phi_N(\mathbf{r}_N), \quad (2.28)$$

where the total energy  $E = \varepsilon_1 + \varepsilon_2 + \dots + \varepsilon_N$  in which  $\varepsilon_i$  represent the energy eigenvalue of each individual  $\phi_i(\mathbf{r}_i)$  and  $\varepsilon_1 < \varepsilon_2 < \dots < \varepsilon_N$ .

From here, under the independent electron approach, we can infer that the lowest energy configuration of the system is reached when one electron fills each state starting from ground state<sup>18</sup>.

It is essential to mention that, although the independent electron give us sense of the energy of the electron, it carries two important drawbacks<sup>18</sup>. First, the wave function  $\Psi$  must obey the Pauli exclusion Principle, which express that function has to change signs whenever we exchange two electrons, and this does not apply to the definition of  $\Psi$  in (2.27). Second, we need to consider that the Coulombic interaction term eliminated from equation (2.17) it is from the same order of magnitude as the rest of them, such it is not negligible. These problems will be treated in the following sections.

### 2.2.3 Hartree-Fock (HF) theory

As mentioned in the previous section, we have two main problems that we need to deal with in this section. On one hand, we must consider the Pauli's exclusion principle, which states: the many-body wavefunction must be anti-symmetric with respect to any pair of electrons, such that the wavefunction changes sign commuting any two electrons. To fulfill this requirement, the simplest ansatz is to rewrite the product many-body wave function as a Slater determinant<sup>21</sup>:

$$\Psi_{HF} = \Psi_{HF}(\mathbf{r}_1\sigma_1, \dots, \mathbf{r}_N\sigma_N) = \frac{1}{\sqrt{N!}} \begin{vmatrix} \phi_1(\mathbf{r}_1\sigma_1) & \phi_1(\mathbf{r}_2\sigma_2) & \dots & \phi_1(\mathbf{r}_N\sigma_N) \\ \phi_2(\mathbf{r}_1\sigma_1) & \phi_2(\mathbf{r}_2\sigma_2) & \dots & \phi_2(\mathbf{r}_N\sigma_N) \\ \vdots & \vdots & \ddots & \vdots \\ \phi_N(\mathbf{r}_1\sigma_1) & \phi_N(\mathbf{r}_2\sigma_2) & \dots & \phi_N(\mathbf{r}_N\sigma_N) \end{vmatrix}, \quad (2.29)$$

where the rows run for the electron and columns for the orbitals<sup>18</sup>. The prefactor with number electrons  $N$  is introduced to correctly normalize the wavefunction. Then, the electron charge

density will come from adding the individual probabilities of finding a electron in  $i$  state, as:

$$n(\mathbf{r}) = \sum_i |\phi_i(\mathbf{r})|^2. \quad (2.30)$$

On the other hand, we have to introduce a term that takes into account the Coulomb repulsion term, while maintaining the single-particle approach. We start considering the electronic charge distribution  $n(r)$ . In classical electrodynamics framework, the electron charge generates an electrostatic potential  $\phi(r)$ , which is replaced for a potential energy  $V_H$  in Hartree units.

$$V_H(\mathbf{r}) = -\Phi(\mathbf{r}) \quad (2.31)$$

This is reflected in the Poisson's equation as:

$$\nabla^2 V_H(\mathbf{r}) = -4\pi n(\mathbf{r}). \quad (2.32)$$

Solving for  $V_H$  we obtain the following solution:

$$V_H(\mathbf{r}) = \int d\mathbf{r}' \frac{n(\mathbf{r}')}{|\mathbf{r} - \mathbf{r}'|}, \quad (2.33)$$

where  $V_H$  is named the Hartree potential. Each of the electrons in the system feel  $V_H$  which is the average potential generated by their charge. This is the mean-field approximation. Taken together the electronic charge density  $n(r)$  and the Hartree potential  $V_H$  we can improve the many-body Schrödinger equation as:

$$\left( -\frac{\nabla^2}{2} + V_n(\mathbf{r}) + V_H(\mathbf{r}) \right) \phi_i(\mathbf{r}) = \varepsilon_i \phi_i(\mathbf{r}), \quad (2.34)$$

Taken together (2.30), (2.33), and (2.34) are the HF equations, necessary to simplify the many body problem as we keep the single-particle framework<sup>18,21</sup>.

The electrons do interact indeed, but this interaction is not too strong, such that we can still look for a solution in the form of a Slater determinant. Then, we find the individual wave functions  $\phi_i$  utilizing the "variational principle"<sup>21</sup>, such that we find the correct ones to minimize the E. This is done considering the total HF wavefunction  $\Psi_{HF}$  on ground state energy. Then, the energy of the system is obtained as:

$$E_{HF} = \int d(\mathbf{r})_1 \dots d(\mathbf{r})_N \Psi_{HF}^* \hat{H} \Psi_{HF} = \langle \Psi_{HF} | \hat{H} | \Psi_{HF} \rangle. \quad (2.35)$$

Equation of the right of (2.35) is described using the Dirac notation, which from now on we will adopt for simplicity. Introducing the requirement that  $\phi_i$  in the Slater determinant (2.29) must be orthonormal, i.e normalized and orthogonal, the calculations are considerably simplified. Then:

$$\langle \phi_i | \phi_j \rangle = \delta_{ij} \quad (2.36)$$

With this condition we consider  $\Psi_{HF}$  automatically normalized.

Notice that equation (2.35) has an implicit dependence on  $\phi_i$ , then we can say that the energy  $E_{HF}$  is a functional of the single-particle wave functions:  $E_{HF} = E_{HF}[\phi_i]$ . Furthermore, we can use this information to incorporate the Lagrange multipliers method that adds the following constrain<sup>18,21</sup>:

$$L[\phi_i, \epsilon_{ij}] = E_{HF}[\phi_i] - \sum_i \epsilon_{ij} [\langle \phi_i | \phi_j \rangle - \delta_{ij}] \quad (2.37)$$

In here,  $\epsilon_{ij}$  act as the Lagrange multipliers, such that the second term disappears due to the orthonormal condition. In Lagrange's method the constrained minimization problem is replaced by:

$$\frac{\delta L}{\delta \epsilon_{ij}} = 0 \quad (2.38)$$

and

$$\frac{\delta L}{\delta \phi_i} = 0 \quad (2.39)$$

Then, we notice two expressions: the Hartree potential (2.33) and a novel term, that we will call the Fock exchange potential:

$$V_X(\mathbf{r}, \mathbf{r}') = - \sum_j \frac{\phi_j^*(\mathbf{r}') \phi_j(\mathbf{r})}{|\mathbf{r} - \mathbf{r}'|}, \quad (2.40)$$

In order to improve the accuracy of our many-body we can take together all the previous results in this section, such that we redefine equation (2.34), as:

$$\left( -\frac{\nabla^2}{2} + V_n(\mathbf{r}) + V_H(\mathbf{r}) \right) \phi_i(\mathbf{r}) + \int d\mathbf{r}' V_X(\mathbf{r}, \mathbf{r}') \phi_i(\mathbf{r}') = \epsilon_i \phi_i(\mathbf{r}), \quad (2.41)$$

In summary, the Hartree Fock theory gives three main equations, expressed in: 2.30, 2.32 and (2.41). Notice that these equations maintain relation with each other; the solutions  $\phi_i$  should

must be such that, if we introduce them in the density charge 2.30 and, consequently, in the Poisson's equation 2.32, the resulting potential  $V_H$  include in (2.41) must give the same  $\phi_i$ . For this reason, this type of approach is named as self-consistent field (SCF) method, which is an iterative procedure that updates the wave functions until it reaches the convergence<sup>18,21</sup>.

## 2.3 Density Functional Theory (DFT) principles

In the previous section we studied the problem of determining the quantum states for N-electron systems, and the extreme challenge that supposes to solve the many-body Schrodinger equation that involves  $3N$  coordinates  $(r_1, r_2, r_3, \dots, r_N)$ . The independent electron approximation allowed to simplify the description of the many-electron system incorporating the product of single-particle wavefunction  $\phi_i$  instead of the complete wavefunction  $\Psi$ . In this section, we will go beyond, studying the Hohenberg-Kohn and Kohn-Sham that provide further and deeper approaches for the many-body problem.

### 2.3.1 Hohenberg-Kohn Theorem

In general, the complexity of the computational calculations for the energy of any quantum state is due to the fact that the energy  $E_0$  is a functional of the entire wavefunction  $\Psi(r_1, r_2, \dots, r_N)$ . This means that to find the  $E_0$  a system of  $3N$  variables must be solved. Hohenberg and Kohn developed an alternative theory though we can calculate  $E_0$  depending on the electron density  $n(r)$ , which depends on 3 variables only. This statement goes under the Hohenberg-Kohn theorem.

In summary:

- Ground state energy  $E$  is functional of  $n(r)$ :

$$E = F[n(r)]$$

- Excited state energy  $E$  is functional of the complete many-body wavefunction  $\Psi$ :

$$E = F[\Psi(r_1, r_2, \dots, r_N)]$$

The proof can be reduced to three statements:

1. The external potential of the nuclei can be determined uniquely by the ground state electron energy:  $n \rightarrow V_n$
2. The many-body wave function is uniquely determined by the external potential:  $V_n \rightarrow \Psi$
3. The total energy is determined by the many body wavefunction:  $\Psi \rightarrow E$
4. Finally, by induction we conclude:  $n \rightarrow V_n \rightarrow \Psi \rightarrow E$ <sup>18</sup> cite HK papers

It is worth mentioning that this simple proof crucially relies on the fact that the energy of the ground state is the lowest possible energy of the system, and all other states are higher in energy. Out of the three statements, the first one is the less intuitive, but it can be proved by *reductio ad absurdum*. Basically, the idea is to start assuming that we can obtain the same ground-state energy  $E$  from two different external potential  $V_n$ , such as this guide us to an absurd<sup>18,21</sup>.

### 2.3.1.1 Hohenberg–Kohn variational principle

Previously in this section it was stated that the ground state energy  $E_0$  can be obtained from a functional depending on the electron density  $n(r)$ . For this to work, the ground state density  $n_0$  has to be the function that will minimize the total energy. This principle can be expressed as the derivative of the functional with respect to the density evaluated exactly in the ground state density:

$$\left. \frac{\delta F[n]}{\delta n} \right|_{n_0} = 0 \quad (2.42)$$

## 2.3.2 Kohn-Sham theory

In previous section, we saw the Hohenberg theorems, however these theorems did not provide any idea on how to construct that functional. In this sense, Kohn and Sham proposed to solve this problem by adding up an exchange and correlation term that would account for the interactions that are not taken into the independent electron approximation.

First, we begin by defining the kinetic energy and the Coulomb energy as operators:

$$\hat{T} = - \sum_i \frac{1}{2} \nabla_i^2, \quad \hat{W} = \frac{1}{2} \sum_{i \neq j} \frac{1}{|\mathbf{r}_i - \mathbf{r}_j|}, \quad (2.43)$$

Using this notation, the energy (2.35) (taking the  $\hat{H}$  in 2.23 and HK theorem) becomes:

$$E = F[n] = \int d\mathbf{r} n(\mathbf{r}) V_n(\mathbf{r}) + \langle \Psi[n] | \hat{T} + \hat{W} | \Psi[n] \rangle. \quad (2.44)$$

The first term depends explicitly on  $n(\mathbf{r})$  while the kinetic and Coulomb term do it implicitly. Kohn and Sham proposed to expand these term and add up an extra exchange correlation term to account for the difference. Then, 2.44 becomes:

$$E = F[n] = \underbrace{\int d\mathbf{r} n(\mathbf{r}) V_n(\mathbf{r})}_{\text{External potential}} - \underbrace{\sum_i \int d\mathbf{r} \phi_i^*(\mathbf{r}) \frac{\nabla^2}{2} \phi_i(\mathbf{r})}_{\text{Kinetic energy}} + \underbrace{\frac{1}{2} \iint d\mathbf{r} d\mathbf{r}' \frac{n(\mathbf{r})n(\mathbf{r}')}{|\mathbf{r} - \mathbf{r}'|}}_{\text{Hartree energy}} + \underbrace{E_{xc}[n]}_{\text{XC energy}} \quad (2.45)$$

Total energy in the independent electron approximation

Here we see all the terms from the independent electron approximation plus the exchange correlation energy  $E_{xc}$ , which contains the all the contributions left out. Then, if we can figure out  $E_{xc}$  it is possible to calculate the ground-state energy by employing the electron density  $n(\mathbf{r})$ . Making use of the Hohenberg–Kohn variational principle we know that the ground-state electron density  $n_0$  minimize the total energy functional  $F[n]$  as in (2.42). Then we can establish the following constrain for the orbitals:

$$\frac{\delta F}{\delta \phi_i^*} = \frac{\delta F}{\delta n} \frac{\delta n}{\delta \phi_i^*} = 0 \quad (2.46)$$

Applying this constrain we obtain a similar problem than in Hartree-Fock theory, which can be approached using the Lagrange multipliers method if we incorporate the functional  $E = F[n]$ . Furthermore, we can apply the HK variational to obtain the individual wave functions  $\phi_i(\mathbf{r})$  in order to build the electron density  $n$ . Then, we obtain:

$$\left[ -\frac{1}{2} \nabla^2 + V_n(\mathbf{r}) + V_H(\mathbf{r}) + V_{xc}(\mathbf{r}) \right] \phi_i(\mathbf{r}) = \epsilon_i \phi_i(\mathbf{r}) \quad (2.47)$$

Where all the terms are identical that in the Hartree-Fock equations just adding up the exchange correlation potential  $V_{xc}(\mathbf{r})$ . This new term is defined as:

$$V_{xc}(\mathbf{r}) = \left. \frac{\delta E_{xc}[n]}{\delta n} \right|_{n(\mathbf{r})} \quad (2.48)$$

The set of equations stated in (2.47) are named the Kohn-Sham equations that constitute the base of the Kohn-Sham theory. In summary, Kohn-Sham theory describes a fictitious system of only electrons that interact through the external potential. The main many-body interaction effects are detailed in the theorem, while the unknown contributions are condensed in the exchange and correlation energy  $E_{xc}$ , and potential  $V_{xc}$ . Then, the accuracy on the calculations performed in DFT will lie heavily on the constructions of the  $E_{xc}$ .

### 2.3.3 Self-consistent calculations

In previous section, we saw the Kohn-Sham equations, that are fundamental ingredients of the Density Functional Theory calculations. In principle, the fundamental idea behind DFT come from applying self-consistent procedure in order to determine, as precisely as possible, the ground-state electron density  $n_0(\mathbf{r})$  and the corresponding energy  $E_0[n]$ . In this sense, we can use the Kohn-Sham equations () to construct a self-consistent algorithm to determine the optimal choice for  $n_0(\mathbf{r})$  and  $E_0[n]$ <sup>18,19</sup>:

1. Calculate nuclear potential  $V_n$  starting from the nuclear coordinates. In general, this information is provided by the crystallography of the material itself.
2. Propose an initial guess for the electron density  $n(\mathbf{r})$ . A suitable approximation is constructed adding up the densities of completely isolated atoms arranged in the atomic positions corresponding to the material.
3. Construct the Hartree and exchange-correlation potentials ( $V_H$  and  $V_{xc}$ ) incorporating the electron density  $n(\mathbf{r})$ .
4. Proceed to find the solutions of the Kohn-Sham equations through numerical methods to find the corresponding wave functions  $\phi_i$ .
5. Use the recently found  $\phi_i$  to construct a better estimate of  $n(\mathbf{r})$  and  $E_0[n]$ .
6. This process is repeated iteratively until the newly calculated  $n(\mathbf{r})$  matches the old one within a certain tolerance. At this point, we say the system reaches the self-consistency. Otherwise, both densities are mixed to obtain a new guess of  $n(\mathbf{r})$  to be introduced in the following iteration.

## 2.4 Exchange-correlation functional $E_{xc}$

DFT has been one of the most studied fields within the materials modelling context, due to this many different of methods have been developed in order to achieve solutions or approximates for real problems. In this sense, we can say that the Kohn-Sham theory along with DFT (KS-DFT), even though it increases the computational cost by several orders of magnitude due to the orbitals incorporation, is one of the most successful and largely used theories in material sciences<sup>22</sup>. Within KS theory, the only part that is still missing is the exchange-correlation energy term  $E_{xc}$ , which is commonly represented as the sum of the exchange functional  $E_x$  and the correlation functional  $E_c$ <sup>23</sup>. With the purpose of finding the optimal functional that fits in any material context to a certain precision approximation methods have been developed, that can be either: non-empirical (satisfy extra constraints) or semi-empirical (undetermined coefficient enhancing)<sup>22</sup>.

Unlike the many-body wave function, DFT is not systematically improvable, i.e. incorporating extra contributions to fit more exact constraints into the model does not guarantee we will get an improvement across all the relevant interactions, this supposes a major complication in DFT. Another possibility to establish a DFT hierarchy was postulated by John Perdew named the "Jacob's Ladder"<sup>24</sup>(Fig. 2.1), which is based on postulations of the Hartree theory: making the exchange correlation energy equal to zero and reducing the interaction between electrons to purely classical<sup>22</sup>. In the following subsection we will overview the four lower rungs of the Jacob's Ladder, putting special attention to the fourth one: Hybrid level which contains the B3LYP functional, which is the functional used in this work.

### 2.4.1 The local spin density approximation (LSDA)

The lowest level of Jacob's ladder is the so called local-spin density approximation (LSDA), the earliest and simplest of all the exchange-correlation energy approximations<sup>23-26</sup>. This approximation is based in consider the material as an electron gas assuming that the density at each point is the same as that of the homogeneous electron gas<sup>27</sup>. As its name states LSDA approximation uses only the local spin densities  $n_\uparrow$  and  $n_\downarrow$  to define exchange-correlation energy  $E_{xc}$  as<sup>23</sup>:

$$E_{xc}^{LSDA}[n_\uparrow, n_\downarrow] = \int d^3r n(\mathbf{r}) \epsilon_{xc}^{unif}(n_\uparrow, n_\downarrow), \quad (2.49)$$

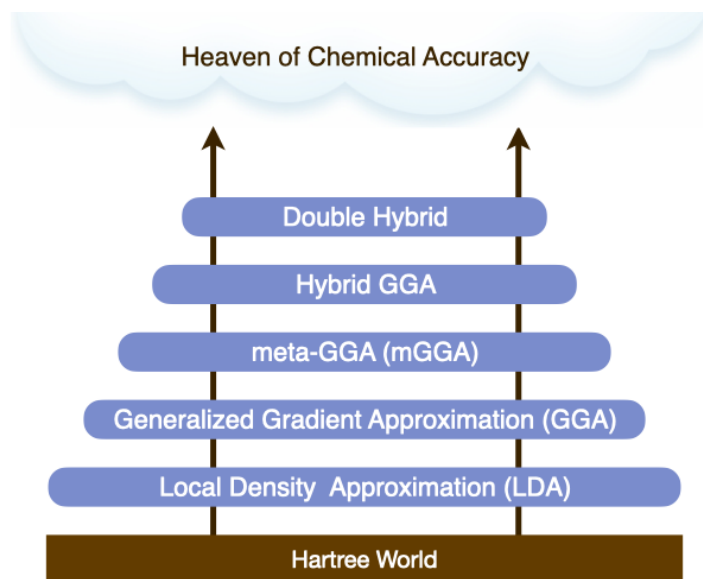


Figure 2.1: Density-functional theory exchange-correlation functional approximations hierarchy according to Jacob's ladder. The base of the ladder is in the Hartree theory (earth) which ascends to the chemical accuracy (heaven). In between there are five defined rungs, ordered according to the precision and amount of contributions incorporated into the functional type. They are sorted in ascending order, introducing in each level extra ingredients into their formulation. Figure adapted from Mandirossian and Head-Gordon<sup>22</sup>

where  $\epsilon_{xc}^{unif}(n_{\uparrow}, n_{\downarrow})$  is the exchange-correlation energy per electron for the uniform electron gas, with evenly distributed  $n_{\uparrow}$  and  $n_{\downarrow}$ . Due to this, LSDA results are successful predicting exactly uniform electron gas properties but fail to predict other real systems as small ensembles of atoms and molecules<sup>24,26</sup>. For example, LSDA is so accurate in the prediction of solids that is still widely, that contrasts with its results of molecular atomization energies, that are unacceptably high<sup>27</sup>. In other words, it is less useful for atoms and molecules, due to they resemble way less to a uniform electron gas.

## 2.4.2 The generalized gradient approximation (GGA)

The second level of Jacob's ladder is the so-called generalized gradient approximation (GGA), which contains an improved version of the LSDA for the exchange-correlation energy<sup>23,24,26,28,29</sup>. In recent years, the GGA functional has become more popular and widely used in solid-state physics and quantum chemistry communities<sup>23,30,31</sup> (see cites of there). This functional incorporates extra terms with respect to the previous level, as we see in the following equation, it includes semi-local information expressed in the gradients of the spin densities<sup>23</sup>:

$$E_{xc}^{GGA}[n_{\uparrow}, n_{\downarrow}] = \int d^3r n(\mathbf{r}) \epsilon_{xc}^{unif}(n) F_{xc}(n_{\uparrow}, n_{\downarrow}, \nabla n_{\uparrow}, \nabla n_{\downarrow}), \quad (2.50)$$

where  $F_{xc}$  is the enhancement factor. The original motivation for the formulation of equation (2.50) came from the second-order gradient expansion (GEA), which was only valid for the slowly varying densities. Then, to solve this problem GGAs introduce additional local density gradients  $\nabla n_{\uparrow}$  and  $\nabla n_{\downarrow}$  in order to account also for the inhomogeneous density distribution problem presented in LSDA<sup>26</sup>.

Even though GGA functional presents an evident improvement in the calculations with respect to LSDA functional, most of the widely used GGAs are still limited<sup>23</sup>. For instance, the PBE functional one of the most popular GGAs predicts lattice constants that are too long and its surface energies and atomization energies are more accurate than LSDA. Then, we can say that GGAs accuracy is reasonable for structures or energies, but not both, in other words: "the GGAs cannot satisfy all the known exact constraints appropriate to a semilocal functional"<sup>23,26</sup>.

## 2.4.3 The meta-GGA

The third level of Jacob's ladder is the so-called meta generalized gradient approximation (mGGA), which is the naturally improved version with respect to the previous level by adding up additional semilocal information<sup>23</sup>. The extra ingredients incorporated are the Laplacian of the density  $\nabla^2 n_{\sigma}$  or the kinetic energy densities  $\tau_{\sigma}$ , obtaining the following form of the functional:

$$E_{xc}^{MGGA}[n_{\uparrow}, n_{\downarrow}] = \int d^3r n(\mathbf{r}) \epsilon_{xc}^{unif}(n) F_{xc}(n_{\uparrow}, n_{\downarrow}, \nabla n_{\uparrow}, \nabla n_{\downarrow}, \nabla^2 n_{\uparrow}, \nabla^2 n_{\downarrow}, \tau_{\uparrow}, \tau_{\downarrow}). \quad (2.51)$$

The Kohn-Sham orbital kinetic energy density for electrons of spin  $\sigma$   $\tau_\sigma$ <sup>27</sup> is defined as:

$$\tau_\sigma(\mathbf{r}) = \frac{1}{2} \sum_\alpha \theta(\mu - \epsilon_{\alpha\sigma}) |\nabla \psi_{\alpha\sigma}(\mathbf{r})|^2, \quad (2.52)$$

where  $\mu$  is the chemical potential. In general, mGGA functionals include either the Laplacian of the density  $\nabla^2 n_\sigma$  or the kinetic energy density  $\tau_\sigma$ , however there are some cases too when it does include both<sup>32,33</sup>. The cases in which  $\tau_\sigma$  is included are predominant and this is due to two main reasons: it arises naturally in the Taylor expansion of the exact spherically averaged exchange hole<sup>34</sup>; it provides a straightforward way to make a correlation functional exactly one-electron self-interaction free<sup>35</sup>. In resume, the incorporation of kinetic energy density  $\tau_\sigma$  provides the mGGA functionals the flexibility to deal with more exact constraints solving the structure-energy dilemma experienced with GGA functionals<sup>23</sup>.

#### 2.4.4 Hybrid functionals

The fourth level of Jacob's ladder is the hybrid functionals<sup>36,37</sup>. At this level, it is necessary to introduce more computationally expensive non-local functionals of the orbitals. In this level, the extra ingredients added to the formulation are the exact exchange energy density or any quantity from which we can obtain it<sup>23</sup>. Then, we shape of the functional is the following:

$$E_{xc}^{MGA}[n_\uparrow, n_\downarrow] = \int d^3r n(\mathbf{r}) \epsilon_{xc}^{unif}(n) F_{xc}(n_\uparrow, n_\downarrow, \nabla n_\uparrow, \nabla n_\downarrow, \nabla^2 n_\uparrow, \nabla^2 n_\downarrow, \tau_\uparrow, \tau_\downarrow, e_x^{exact}). \quad (2.53)$$

where

$$e_x^{exact}(r) = \frac{1}{2} \sum_\sigma \int d^3r' \left( \frac{n_\sigma}{n} \right) \frac{n_x(r'\sigma, r\sigma)}{|r' - r|} \quad (2.54)$$

The exact energy density  $e_x^{exact}(r)$  can be calculated from the occupied Kohn Sham orbitals<sup>27</sup>.

Another way to write the hybrid functional is a simpler way is to do it in terms of the previous functionals, such as we express the hybrid functional including the fraction of the exact exchange mixed with GGA exchange and correlation parts:

$$E_{xc}^{hyb} = aE_x^{exact} + (1 - a)E_x^{GGA} + E_c^{GGA}. \quad (2.55)$$

where the constant  $a$  can be fitted empirically or estimated theoretically. Some of the most famous hybrid functionals include the B3LYP, B3PW91, or PBE0, that combine a determinate

fraction of exact exchange with some GGA exchange and local hybrids. In general, global hybrid functionals are remarkably accurate in the prediction of molecules and strongly inhomogeneous solids, however, they do not satisfy any exact-constraint that is not already solved with standard GGAs<sup>26</sup>. Despite this fact, Hybrid functionals are the most accurate density functionals in use for quantum chemical calculations<sup>27</sup>.

In this work we will focus on the B3LYP hybrid functional, which stands for Becke 3-parameter Lee–Yang–Parr, which is expressed in terms of GGAs and LSDAs, as:

$$E_{xc}^{B3LYP} = (1 - a)E_x^{LSDA} + aE_x^{HF} + b\Delta E_x^B + (1 - c)E_c^{LSDA} + cE_c^{LYP}, \quad (2.56)$$

where  $a = 0.20$ ,  $b = 0.72$ , and  $c = 0.81$ , the three parameters that give name to the functional. The exchange part is given by the Becke 88 exchange functional  $E_x^B$ <sup>38</sup>, while the correlation part is given by the Lee, Yang and Parr correlation functional<sup>39</sup>, taken together we get B3LYP. Additionally, we have  $E_x^{LSDA}$  and  $E_c^{LSDA}$  the local-spin density exchange and correlation functionals, respectively<sup>40</sup>.

## 2.5 Basis set

From the mathematical point of view, a basis set is defined as a collection of vectors that can describe a complete space on which a problem is solved. Making this analogy, a basis set in quantum computation can be seen as the one- particle function, such that a combination of them constitutes molecular orbitals. In principle, all *ab initio* methods incorporate a certain basis set depending on the calculations that will be performed, due to each basis set being optimized for different purposes. Since the molecular orbitals are described by the basis set, the smaller that basis set is the poorer is the representation of the orbital, in other words, they have a considerable influence on the accuracy of the calculations<sup>41</sup>. For instance, it is known that the computational effort of *ab initio* methods scales as at least  $M_{basis}^4$ , then it is essential to choose the basis set as small as possible, such that it does not compromise the accuracy of the calculations<sup>42,43</sup>.

Additionally, basis sets need to accomplish the following constraints<sup>41</sup>:

- Basis sets are formulated such they reflect the nature of the problem they treat, providing good accuracy in the calculations with few functions.
- Basis sets should be available in several hierarchical levels.

- Basis sets should converge relatively fast and monotonically.
- Basis set should be optimized to deliver the target accuracy with the less computational cost possible.
- Basis sets should ideally be universal, which means they have to be appropriate for different methods and properties,
- Be available for all atoms, or at least for a large fraction of the periodic table.

There exist different types of basis sets, such as the Slater-Type orbitals (STO), Def2, the Gaussian-Type orbitals (GTO), etc. In this work, we will focus on GTO, due to it is the one that was incorporated in our calculations.

### 2.5.1 Gaussian-Type orbitals

The Gaussian-type orbitals<sup>4</sup> are described in terms of the Cartesian coordinates as<sup>41</sup>:

$$\chi_{\xi, l_x, l_y, l_z}(x, y, z) = N x^{l_x} y^{l_y} z^{l_z} e^{-\xi r^2} \quad (2.57)$$

In this case, the  $l_x$ ,  $l_y$ , and  $l_z$  in Eq.2.57 would represent the parameters that determine the type of orbital. If we sum them up as we would obtain the angular momentum of the atom  $L = l_x + l_y + l_z$ . It is known that the  $r^2$  dependence in Eq.2.57 affects the GTO in two specific ways: (i) GTO has zero slopes, then it is difficult to study the behavior near the nucleus; (ii) GTO will fall off exponentially from then nucleus, making the representation of the wavefunction deficient<sup>41</sup>. In any case, GTO is able to form a complete set, but due to the constraints explained above, it will need more functions in order to achieve the desired accuracy, in comparison to other basis sets. However, this is compensated widely by the ease with which the required integrals can be calculated<sup>41</sup>. For this main reason, the GTOs are the preferred basis set in molecular electronic structure calculations.

## 2.6 RIJCOSX Algorithm

The RIJCOSX algorithm is an approximation mainly used to speed up Hartree–Fock (HF) and hybrid density functional calculations<sup>44,45</sup>. This is done by building the Coulomb and exchanging

parts of the Fock matrix with different approximations. First, the RI-J algorithm is in charge of dealing with the Coulomb interaction, specifically, computing the near-field part calculations with Gaussian basis functions. For instance, this algorithm is specially suitable for basis sets that have many high angular momentum functions<sup>45</sup>. Second, we have the Chain-of-Spheres Exchange (COSX) algorithm which is in charge of implementing a semi-numerical integration techniques and density fitting for the exchange matrix<sup>46</sup>. Then, the combination of the COSX exchange algorithm with the RI-J approximation for the Coulomb term is called RIJCOSX.

## 2.7 Tight Binding (TB)

In solid-state physics, the tight-binding model (TB) is an approach to calculate electronic-structure properties of crystals and big molecules. The fundamental idea behind is TB model is using an approximate basis set of wave functions considering they are in superposition within each other. The overlapping of the wavefunction leads us to the energy level, such that for an N-atoms system, N orbitals are formed for each orbital in the atom<sup>20</sup>. Taking this into count, we can say that there are allowed and forbidden regions of energy for all the solids, and this already is a prediction of the TB model<sup>20</sup>.

Density-functional Tight Binding (DFTB) methods represent a semi-empirical approximation to the latter. For instance, the total energy is represented through a Taylor expansion around  $\Delta\rho = 0$ <sup>47</sup>:

$$E[\rho] = E^{(0)}[\rho_0] + E^{(1)}[\rho_0, \delta\rho] + E^{(2)}[\rho_0, (\delta\rho)^2] + E^{(3)}[\rho_0, (\delta\rho)^3] + \dots \quad (2.58)$$

## 2.8 Molecular Dynamics (MD) theory

Classical molecular dynamics is a well-known and widely implemented process of computational chemistry and materials modeling. In principle, MD follows a well-defined procedure, integrating numerically Newton's equations of motion for the atoms in the system. In order to perform a proper MD it is necessary to set some constraints according to the purpose of the study, such as the type of ensemble we will use and the time step of the MD. For instance, the time step is usually determined by the highest frequency motion of the system<sup>48</sup>. Typically, the most important output

of MD are the distributions of nuclear positions, velocities, and forces, hence, it is essential to ensure that the initial configuration is not biased in any way.

### 2.8.1 Verlet algorithm

Verlet algorithm is implemented in order to obtain the position updates of the atoms from the forces involved in the MD. In this procedure it is necessary to solve the Newtons' equations of motion, however, for any physical system with a certain level of complexity, these equations are far too completed, then, it is more convenient to consider the numerical integration instead. A simple way to do this is to use the Taylor expansion<sup>19</sup>:

$$r_i(t + \Delta t) = r_i(t) + \frac{dr_i(t)}{dt}\Delta t + \frac{1}{2}\frac{d^2r_i(t)}{dt^2}\Delta t^2 + \frac{1}{6}\frac{d^3r_i(t)}{dt^3}\Delta t^3 + O(\Delta t^4) \quad (2.59)$$

Rewriting this equation in terms of the derivatives we get:

$$r_i(t + \Delta t) = r_i(t) + v_i(t)\Delta t + \frac{1}{2}a_i(t)\Delta t^2 + \frac{1}{6}\frac{d^3r_i(t)}{dt^3}\Delta t^3 + O(\Delta t^4) \quad (2.60)$$

If we express this equation with a negative and positive time step and take the difference, we obtain than:

$$r_i(t + \Delta t) \approx 2r_i(t) - r_i(t - \Delta t) + \frac{F_i(t)}{m_i}\Delta t^2 \quad (2.61)$$

This is the so-called Verlet algorithm. Notice that providing a sufficiently small  $\Delta t$  we can obtain an accurate approximation to the true trajectory<sup>19</sup>.



# Chapter 3

## Methodology

In this chapter, we will present a detailed description of all the processes implemented in this work. It is separated into two main sections: (i) Computational modelling methods, in which we will describe the soft-wares used to process the clusters; (ii) Computational procedure for cluster development, in which we will describe in detail the different processes the clusters went through and the selection criteria for them.

### 3.1 Computational modelling methods

#### 3.1.1 Extended tight-binding (*xTB*) package

Extended tight binding is a semi-empirical quantum mechanical method (GFNn-xTB) which basis wave functions<sup>5</sup> consists in a minimal valence set of atom centered, contracted Gaussian functions<sup>49</sup>. GFNn-xTB methods incorporate electrostatic interactions and exchange-correlation effects up to second order when we need to deal with multipole expansion<sup>49,50</sup> and unlike other semi-empirical methods xTB incorporate a solid strategy with global and element-specific parameterization. In particular, this method focus specially in properties such as energy minimization, geometries, vibrational frequencies, and non-covalent interactions. Considering this GFNn-xTB methods are very well suited for simulating structures with molecular dynamics<sup>51</sup>. In this work we take advantage of this feature by applying a molecular dynamics process to our  $TiO_2$  nanoclusters.

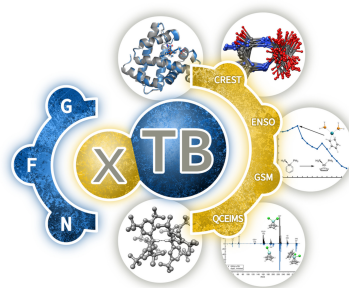


Figure 3.1: Extended tight binding GFNn-xTB logo<sup>5</sup>.

### 3.1.2 ORCA

ORCA is a general-purpose *ab initio* quantum chemistry program package developed in 1999 by Frank Neese investigation group that implements virtually all modern electronic structure methods, in particular, we are interested in the density functional theory semi-empirical methods<sup>6</sup>. ORCA uses standard Gaussian basis functions and is fully parallelized. In this work ORCA is implemented to accurately perform extensive relaxation over sets of nanoclusters and calculate its corresponding electronic properties.



Figure 3.2: ORCA logo<sup>6</sup>.

## 3.2 Computational procedure for cluster development

In this subsection, we will explore step-by-step the process applied to each of the  $TiO_2$  nanoclusters in order to obtain their electronic structure and other physical properties. To achieve this goal, a general overview of the thesis procedure and methodology is outlined in Fig.3.3. Each of the

steps will be developed in more detail in the following sections.

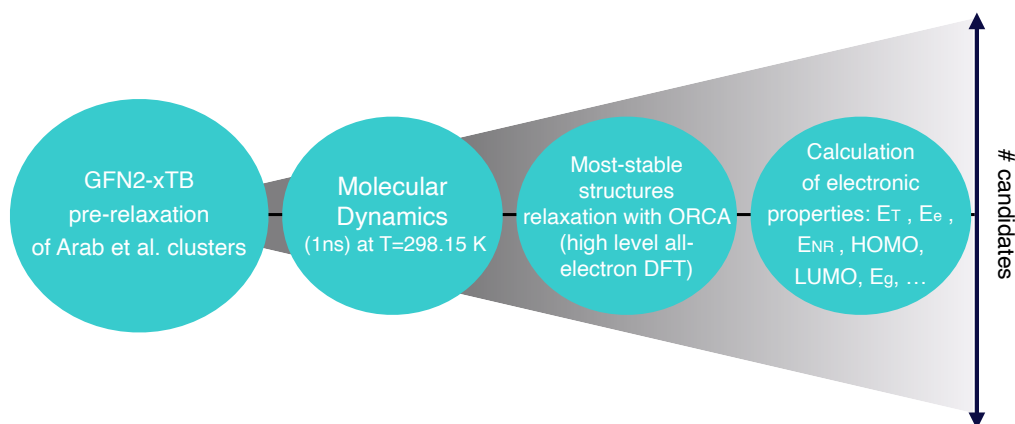


Figure 3.3: Schematic diagram of the process followed to obtain the electronic structure and other physical properties from  $(TiO_2)_n$  ( $n = 1-10$ ) nanoclusters obtained originally from Arab et al.<sup>15</sup>

### 3.2.1 Construction of the clusters in ASE

As a first step, it was necessary to make a proper selection of the clusters that we going to be processed in this work. In this sense, we extracted the original structure from Arab et al.<sup>15</sup> where a variety of clusters  $(TiO_2)_n$  ( $n = 1 - 10$ ) is presented, then we selected the clusters making sure to take at least one of each  $n$ . Although, in this work a total of 27 clusters were processed following exactly the same steps, for illustrative purposes we will just present the 6f2 cluster in this section.

Once the selection was completed, we proceeded to the construction itself of the clusters, transforming the 2D information in Arab et al. into 3D models that we are able to manipulate. For this purpose, we made use of the ASE software, which is widely used in the materials modelling field and was convenient for us due to its intuitive and user-friendly interface. When we are satisfied with the modelling of the clusters we save the ase files in Protein Data Bank

(.pdb) format, for example: 6f2.pdb. Then, in order to make sure the integrity of the file was not corrupted we open up 6f2.pdb and save it once again in turbomole format, as 6f2.turbomole. Finally, we open up again the 6f2.turbomole file and save it in Cartesian coordinates format .xyz as 6f2.xyz (Fig. 3.4). This last will be the actual format that we will use from now on to describe the positions of the atoms in the cluster. To save time we also open *ase* files by simply typing the command line in Fig.3.5.

### 3.2.2 xTB pre-relaxation and Molecular Dynamics (MD).

Once we had the initial structure of the cluster we proceeded to perform on it a subtle pre-relaxation using the xTB software. The command line to run this optimization is presented in Fig.3.6. We obtain a *xtbopt.xyz* file once the pre-relaxation is done. A comparison between before and after the pre-relaxation is presented in Fig.1, where we can easily notice a considerable difference between before and after the process.

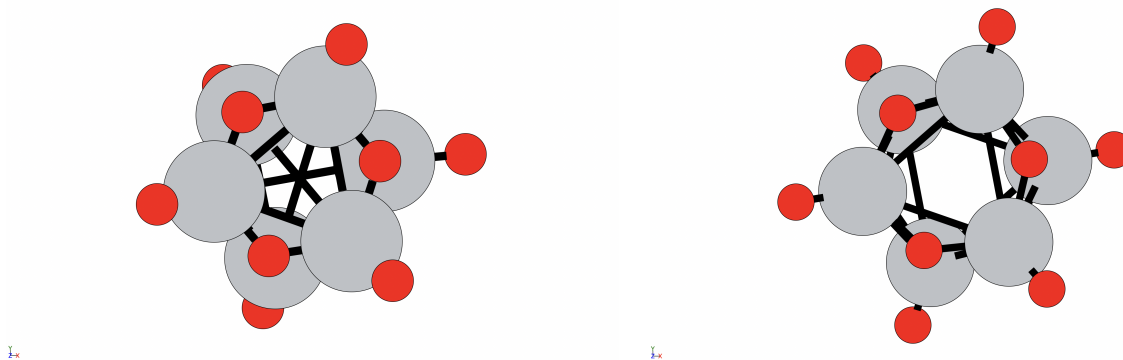


Figure 1. Before (*left*) and after (*right*) pre-relaxation in xTB package.

Following this, we proceed to perform a Molecular Dynamics (MD) simulation on the system. The MD calculations are done with the xTB software using Gaussian basis wave functions at room temperature ( $T = 278.15$  K), for a total time of 1 nanosecond (ns). In this case, we occupy the canonical type of ensemble (NVT), in which the amount of substance (N), volume (V) and temperature (T) are conserved. All the previous parameters are expressed in the *md.inp* file (Fig.3.7). Taken together the *xtbopt.xyz* and *md.inp* are the input files to perform our MD.

```
1 18 # number of atoms
2 Element      x              y              z
3 O      -4.98800000    2.87200000    -0.65000000    8
4 Ti     -3.97400000    1.72300000    -0.49500000    22
5 O     -2.47300000    2.03500000    -0.34600000    8
6 Ti     -1.98600000    3.49600000    -0.35100000    22
7 O     -3.00000000    4.64500000    -0.50600000    8
8 Ti     -4.50100000    4.33300000    -0.65500000    22
9 Ti     -5.08700000    2.94000000    1.04300000    22
10 O     -4.09300000    1.76600000    1.11100000    8
11 Ti     -2.58300000    2.04100000    1.24200000    22
12 O     -2.06800000    3.49100000    1.30300000    8
13 Ti     -3.06200000    4.66500000    1.23500000    22
14 O     -4.57100000    4.39000000    1.10400000    8
15 O     -1.83000000    1.31700000    1.96800000    8
16 O     -6.12700000    2.70200000    1.67200000    8
17 O     -2.67800000    5.62200000    1.71600000    8
18 O     -4.19700000    0.81700000    -1.26100000    8
19 O     -4.92700000    4.87600000    -1.65900000    8
20 O     -0.50200000    3.61700000    -0.99200000    8
21
```

Figure 3.4: 6f2.xyz GFNn-xTB input file.

```
username:~$ ase gui -b 6f2.pdb
```

Figure 3.5: Command line for opening ASE.

```
username:~$ xtb 6f2.xyz --opt tight -P 4 > results.out
```

Figure 3.6: Command line for pre-relaxation performed in xTB with 4 cores.

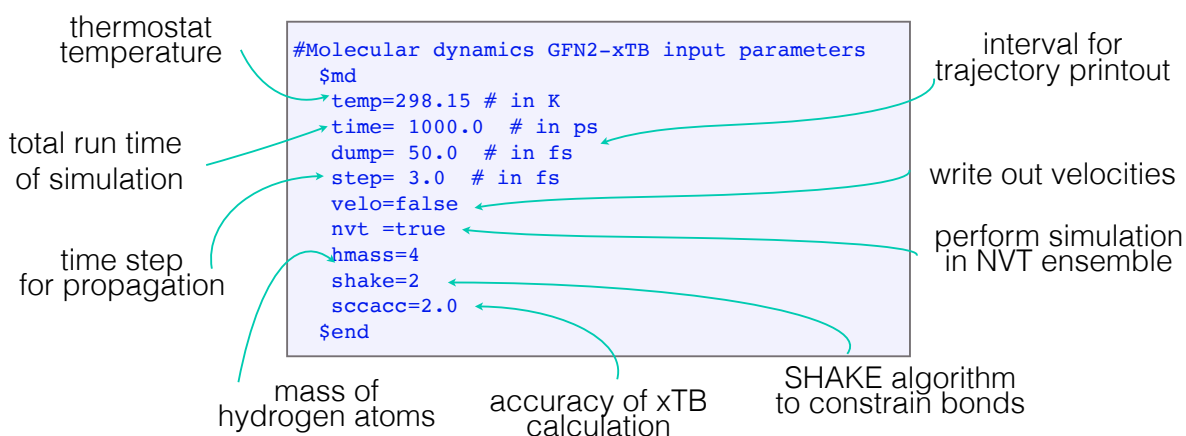


Figure 3.7: A production input file used in GFN2-xTB to compute the molecular dynamics in  $TiO_2$  nanoclusters.

Afterwards, the MD is finished we obtain different output files, describing the topology, charges, as well as the trajectory followed by the cluster, thought the simulation time (*xtb.trj*) which is simply a *.xyz* file repeated as many times as indicated in the *md.inp* file. The total energy of the cluster in each specific configuration per step is also computed and plotted in Fig.3.8. In here, we can notice some particular configurations of the clusters as the time passes. Specifically, in *6f2* cluster, we can easily see a "stairs-kind of behavior" where the three most stable phases are present, one per stair, and are pointing to the specific peak of energy where they are generated. These three phases are topologically different from each other and correspond to a single original

cluster. We collected these most-stable configurations for each of the clusters to follow with the next step of the processing.

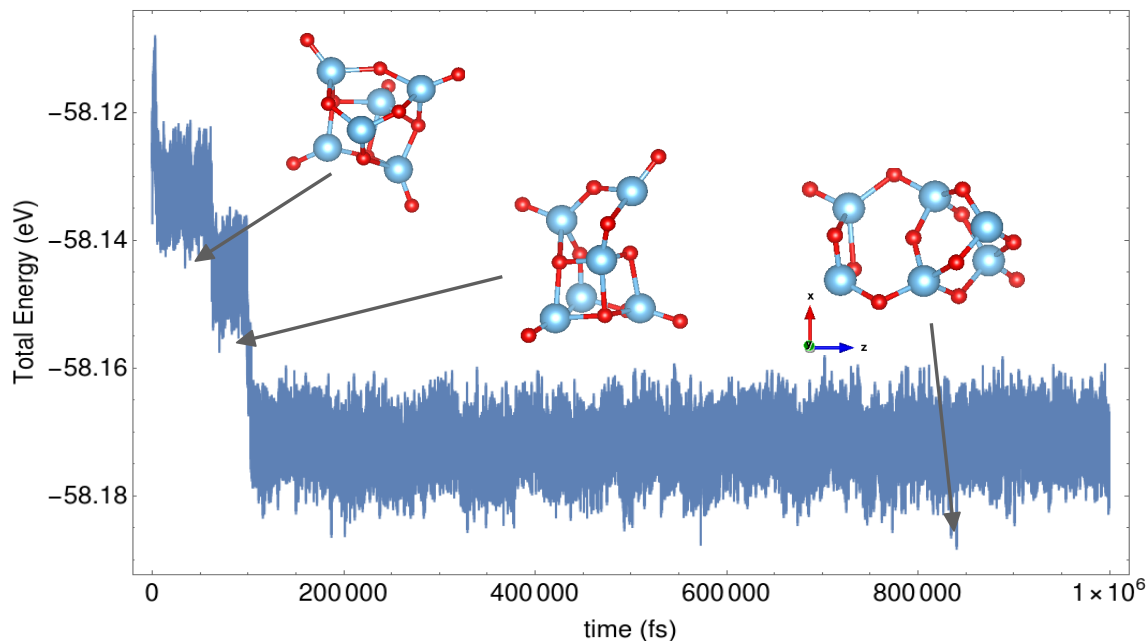


Figure 3.8: Molecular dynamics (MD) at room temperature ( $T = 298.15$  K) for 1 ns of  $6f2 TiO_2$  nanocluster. Notice the MD reaches the energy equilibrium, the structure stabilizes to a defined range of energies for a period of time. In each of the stair-like regions the nanocluster remains with a certain topology and it is pointing with an arrow to the correspondent energy peak in which it is present, such that the they are the most stable configurations of each of their regions. Notice that after two stair-like region we get a lowering in the range of the energies (phase transition) and it is maintained for the rest of the MD time.

### 3.2.2.1 How to choose the time step $\Delta t$ for the MD?

In order to perform a proper MD, it is necessary to select the proper time step for propagation, which will depend on the type of molecules or atoms we are simulating. The vibration frequency of the atom and the time step for propagation have an inverse relationship, which means that for atoms with high-frequency vibrations it is more convenient to use a low time step, such we are

able to catch the rapid vibrations of the atom. For example, in the case of the Hydrogen atom which are the lightest atoms in nature, the time step will have to be the lowest possible (0.5-1 fs). For our particular case, we are dealing with  $TiO_2$  clusters, which means we have heavy atoms like  $O$  and  $Ti$ . Then, we performed a series of MD with different time steps to the same nanocluster structure:  $4c2$ . It is worth mentioning that the computational cost of the calculations increases with lower time steps, taking this in count the selection criteria is to take the highest time step that still catches the phase transitions and reaches the convergence in the calculations. The set of MD performed on  $4c2$  nanocluster is presented in Fig.3.9.

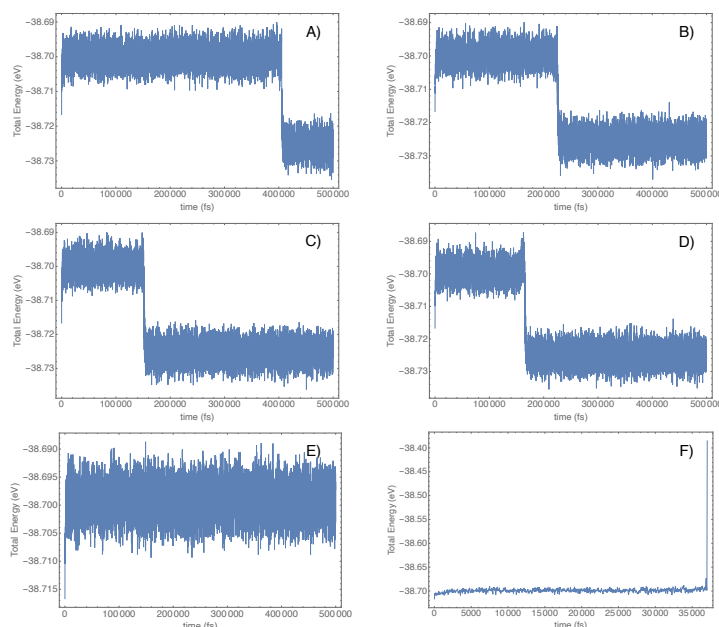


Figure 3.9: Molecular dynamics (MD) of  $4c2$  nanocluster at room temperature ( $T = 298.15$  K) for 0.5 ns , where each of the MD graphs correspond to an specific  $\Delta t$ . **A** : 1 fs; **B** : 2 fs; **C** : 3 fs; **D** : 4 fs; **E** : 5 fs; **F** : 7 fs.

Notice that as we increase the time step the phase transition occurs earlier in the total MD time until we reach to the  $\Delta t = 4$  fs which maintains the phase transition at almost the same level as in  $\Delta t = 3$  fs (Fig.3.9 C-D). Going to higher time steps we miss the phase transition (Fig.3.9 E), furthermore, we do not reach an energetic convergence (Fig.3.9 F). Applying the phase transition

and energetic convergence criteria for the selection of the proper  $\Delta t$ , it is straightforward to conclude that our optimal time step would be  $\Delta t = 3-4$  fs (Fig.3.9 C-D). Since we will be dealing with larger and more complex nanoclusters than  $4c2$ , we selected  $\Delta t = 3$  fs for extra safety.

### 3.2.3 ORCA relaxation

In order to calculate the different electronic properties, it is essential to perform a proper relaxation to each set of stable structures per cluster of  $(TiO_2)_n$ . In this part we chose an all-electron relaxation for our case. Then, for this purpose, we set up a code in ORCA<sup>6</sup> an *abinitio* molecular dynamics semi-empirical package, in order to ensure a much more extensive relaxation in comparison with the pre-relaxation performed at the beginning.

Following the extensive relaxation process, we can finally begin to calculate the electronic properties of the most-stable clusters. In particular, this code implements the high-level calculations of B3LYP hybrid functional within the RIJCOSX approximation with def2-TZVPP basis set and def2/J auxiliary basis set. An overview of the input file is sketched in Fig.3.10

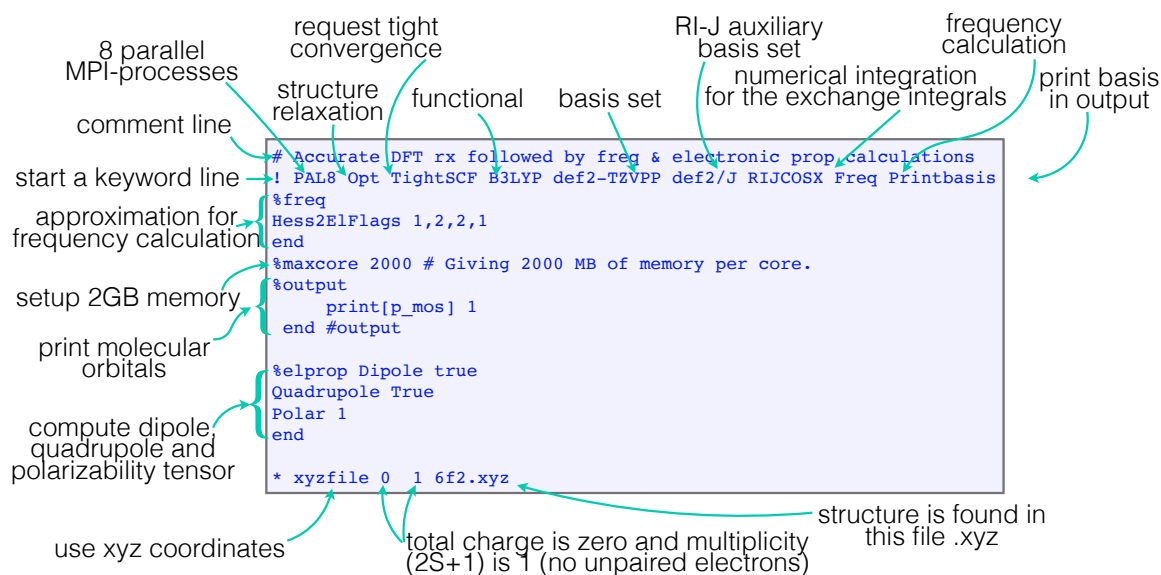


Figure 3.10: A production input file used in ORCA to compute the relaxation and the electronic properties of the cluster.

ORCA generates a list of files, but the most important for our purposes are the `6f2.out` file,

within all the information is extensively detailed, and the *6f2.xyz* file, which contain the relaxed cluster coordinates. The electronic properties we aimed to obtain are detailed in the *6f2.out* file, then, we need to extract the relevant information from there. The results that are relevant for this work are<sup>52</sup>:

- The electronic energy ( $E_{elec}$ ): describes the electrostatic repulsion between the electrons.
- The nuclear repulsion energy ( $E_{NR}$ ): describes the electrostatic repulsion between the nuclei and it is independent of the electron coordinates.
- The Dipole moment ( $D$ ): They occur when there is a separation of charge and it is a measure of the polarity of the molecule.
- The Quadrupole moment ( $Q$ ): It is related to the shape of the nucleus and it indicates the departure of nuclear charge from spherical symmetry.
- The Polarizability ( $P$ ): Tendency of matter to acquire an electric dipole moment in presence of an electric field.
- The zero-point energy ( $E_{ZP}$ ): It is the lowest possible energy that a quantum mechanical system may have represented by vibrations retained even at the absolute zero of temperature.
- The total energy of the system ( $E_{tot}$ ): Summation of all the energy contributions explained above.
- The highest occupied molecular orbital energy (HOMO)
- The lowest unoccupied molecular orbital energy (LUMO)
- The HOMO-LUMO energy gap ( $E_g$ ): Energy difference between HOMO-LUMO orbitals.
- The Gyration radius ( $R_g$ ): The root-mean-square average of the distance of all scattering elements from the center of the mass of the cluster.

# Chapter 4

## Results & Discussion

In this section, we will discuss the outcome of the semi-empirical MD simulations followed by *ab initio* relaxation that we used to predict physical properties. It is important to stress that despite a typical MD simulation requires a period of equilibration, we decided to consider all the structures obtained during the 1 ns. Nonetheless, we only analyze the electronic structure of the most stable phases of the MD as we expect that structure to be the most likely found at 298.15 K.

### 4.1 Molecular dynamics simulations and electronic structure of $(\text{TiO}_2)_n$ , $n = 1 - 10$ clusters and electronic distribution calculations.

In this section is presented the results of the NVT molecular dynamics simulations (MD) at room temperature for 1 ns and parallel it is analyzed the HOMO distribution in each of the cases.

Figure 4.1 displays the outcome of the MD for  $n = 2$  clusters. Notice that none of the three cases show phase transitions, keeping an linear-like structure during all the MD. Nonetheless, the effect of the temperature allows those clusters to explore more stable configurations leading to the same structure despite the different initial configuration (*cf.* Table 4.1: 2a1, 2a2 and 2a3 along the original structure column); this trend is clearly observed in Table 4.2, where the  $E_{tot}$  for these structures are -1999.951 Ha and  $R_g \sim 1.6$  Å. The B3LYP computed electronic structure shows the HOMO formed mainly by O-2p states.

4.1. MOLECULAR DYNAMICS SIMULATIONS AND ELECTRONIC STRUCTURE OF  
38  $(TiO_2)_N$ ,  $N = 1 - 10$  CLUSTERS AND ELECTRONIC DISTRIBUTION CALCULATIONS.

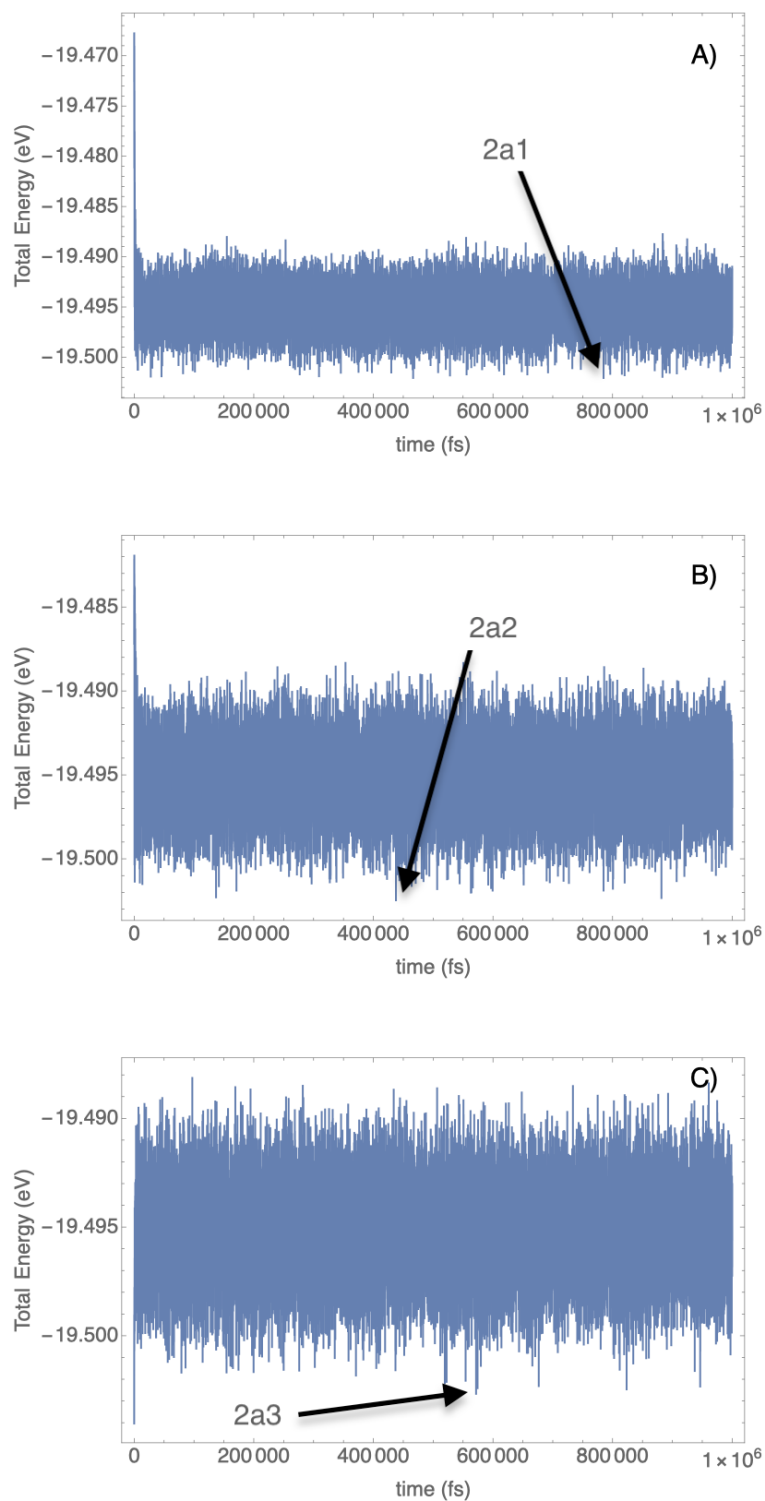


Figure 4.1: Molecular dynamics of  $(TiO_2)_2$  nanoclusters. **A** : 2a1; **B** : 2a2; **C** : 2a3.

Figure 4.2 displays the outcome of the 1 ns MD for  $n = 3$  clusters. The MD simulation yields a linear-like structure for all the clusters. Nonetheless, HOMO distribution displays O-2p states located along the O atoms that are lying in the same plane (Table 4.1). In particular, we notice that 3b1, 3b3 and 3b4 clusters converged to practically the same configuration after the relaxation; this can be also observed in Table 4.2 were despite those structures have an  $E_{tot}$  of  $\sim 3000$  Ha and  $R_g \sim 1.9$  Å.

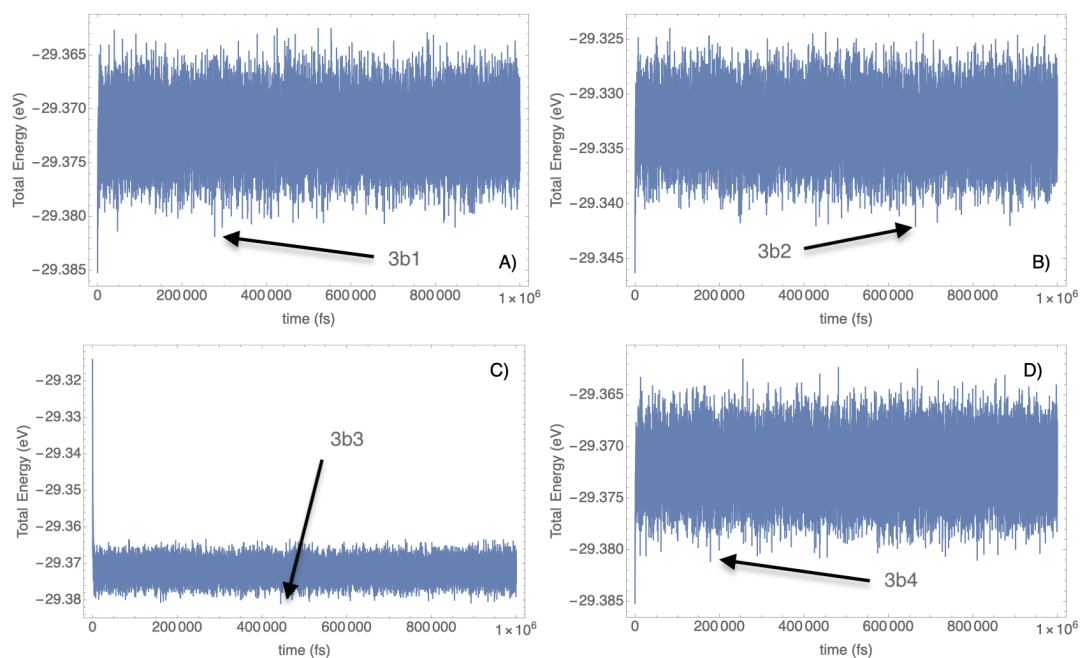


Figure 4.2: Molecular dynamics of  $(TiO_2)_3$  nanoclusters. **A** : 3b1; **B** : 3b2; **C** : 3b3; **D** : 3b4.

Figure 4.3 displays the outcome of the 1ns MD for  $n = 4$  clusters. The MD simulation yields two pairs of similar structures: 4c1c and 4c2b; 4c3 and 4c4, that are stair-like. In 4c1 MD (Fig.4.3 A) there are three well-defined phases, each of them considerably separated in energy, one at the very beginning and the most stable one almost at the end. In 4c2 MD (Fig.4.3 B) there are two well-defined phases. Meanwhile, 4c3 and 4c4 MDs yield linear-like structures thought all the MD time. Furthermore, notice in Table 4.1 that after relaxation all of them converge to the same configuration, which makes sense due in Table 4.2 it is stated that  $E_{tot}$  for these structures are

4.1. MOLECULAR DYNAMICS SIMULATIONS AND ELECTRONIC STRUCTURE OF  
40  $(TiO_2)_N$ ,  $N = 1 - 10$  CLUSTERS AND ELECTRONIC DISTRIBUTION CALCULATIONS.

-4000.079 Ha.

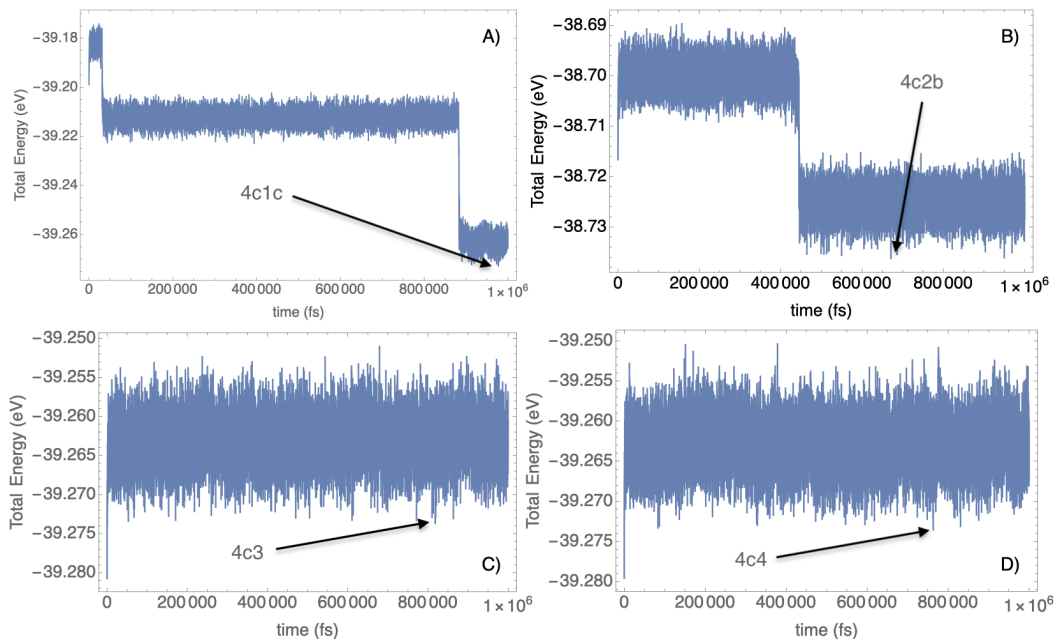


Figure 4.3: Molecular dynamics of  $(TiO_2)_4$  nanoclusters. **A** : 4c1; **B** : 4c2; **C** : 4c3; **D** : 4c4.

Figure 4.4 displays the outcome of the 1ns MD for  $n = 5$  clusters. The MD simulation yields two similar structures (5d2 and 5d3). In 5d2 MD (Fig.4.4 B) there are three stair-like structures, one occurring at the very beginning of the MD time, and it presents some energy fluctuations in the most-stable phase. In 5d3 MD (Fig.4.4 C) there are also three stair-like structures, one occurring at the very beginning of the MD time. Notably, the energy difference from one phase to the other is considerable in this case. At last, we have a linear-like structure in 5d1 MD, that particularly presents some fluctuations at the beginning. Additionally, 5d1, 5d2, and 5d3 converge to the same configuration after relaxation (Table 4.1); this trend is also observed in Table 4.2 since the  $E_{tot}$  for these structures is around -5000.156 Ha, and  $R_g \sim 2.6$ . Also, note that HOMO distribution displays O-2p states located along with the O atoms.

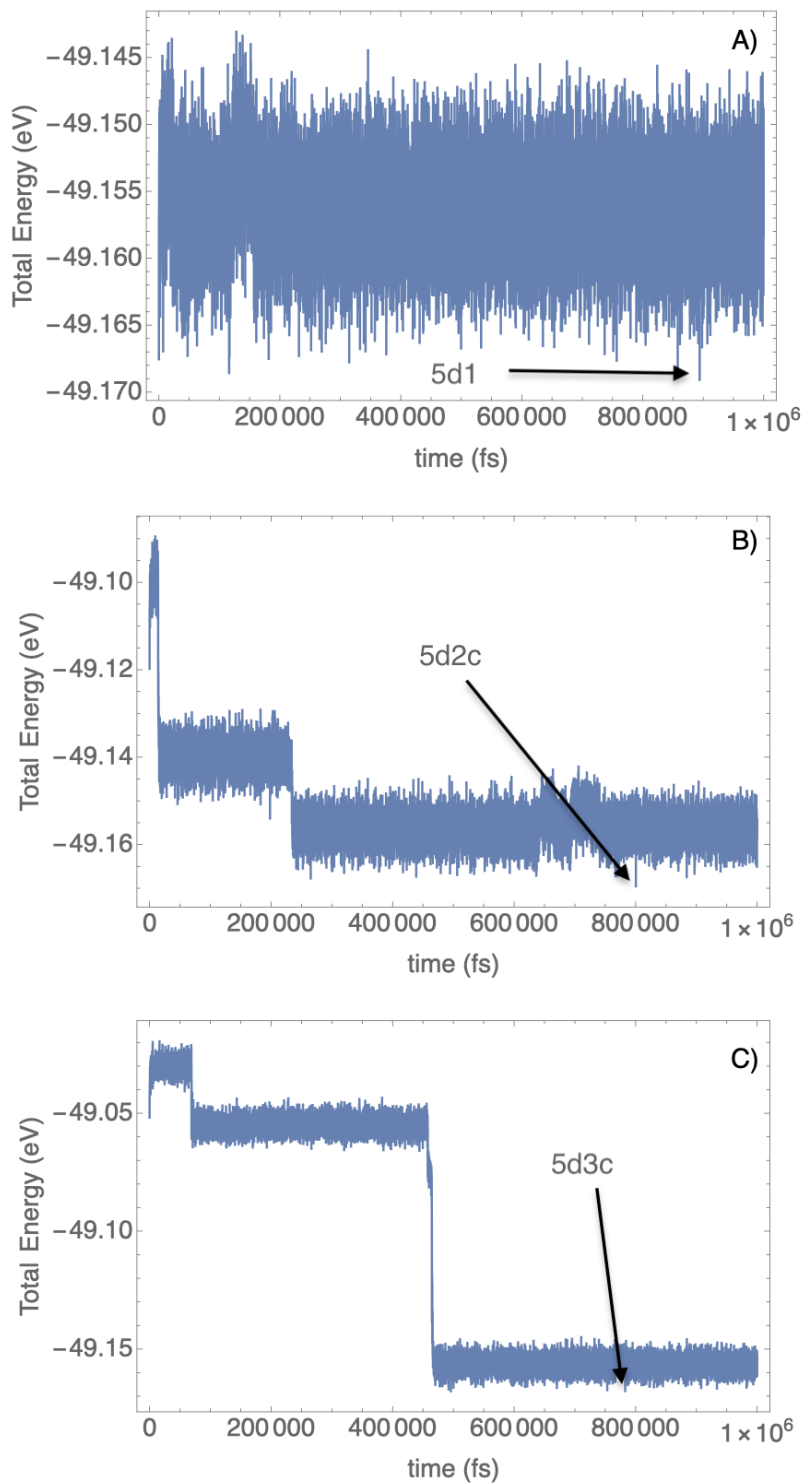


Figure 4.4: Molecular dynamics of  $(TiO_2)_5$  nanoclusters. **A** : 5d1; **B** : 5d2; **C** : 5d3.

#### 4.1. MOLECULAR DYNAMICS SIMULATIONS AND ELECTRONIC STRUCTURE OF $(TiO_2)_N$ , $N = 1 - 10$ CLUSTERS AND ELECTRONIC DISTRIBUTION CALCULATIONS.

Figure 4.5 displays the outcome of the 1 ns MD for  $n = 6$  clusters. First of all, we can notice some very specific phase transitions for both 6f structures. In 6f1 MD (Fig.4.5 A) there are four stair-like structures. In particular, there is one less-stable phase transition just after the original one. In 6f2 MD (Fig.4.5 B) there are three stair-like structures. Notice that we get two rapid phase transitions at the very beginning and then it reaches the most-stable phase for most of the MD time. Furthermore, notice in Table 4.1 the HOMO distribution is mainly formed by O-2p states.

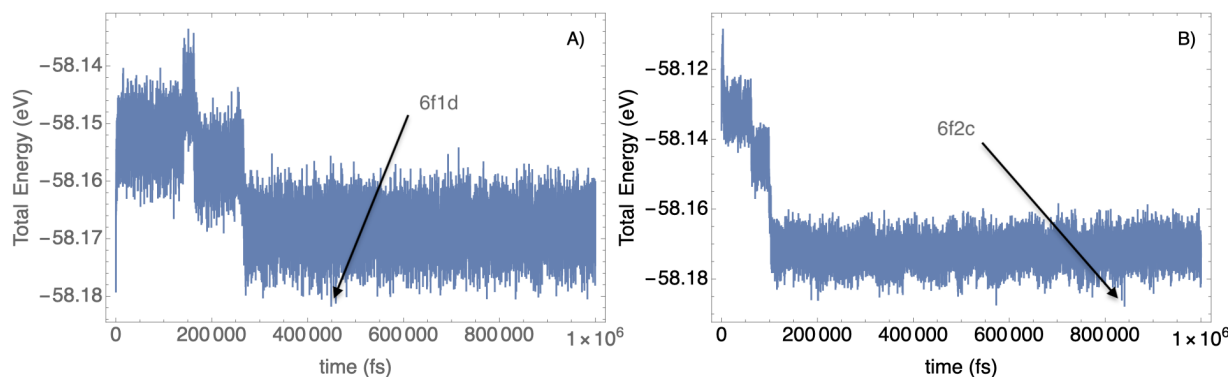


Figure 4.5: Molecular dynamics of  $(TiO_2)_6$  nanoclusters. **A** : 6f1; **B** : 6f2.

Figure 4.6 displays the outcome of the 1 ns MD for  $n = 7$  clusters. The MD simulation yields two similar structures (7g1 and 7g2) which are linear-like structures, however, 7g2 MD has a particular shape that, although it does not become a phase transition, show a vibration-like shape. Meanwhile, in 7g3 MD it is clear the presence of the a single well-defined phase transition. Additionally, note in Table 4.1 that the major contribution to HOMO orbitals distribution are O-2p states.

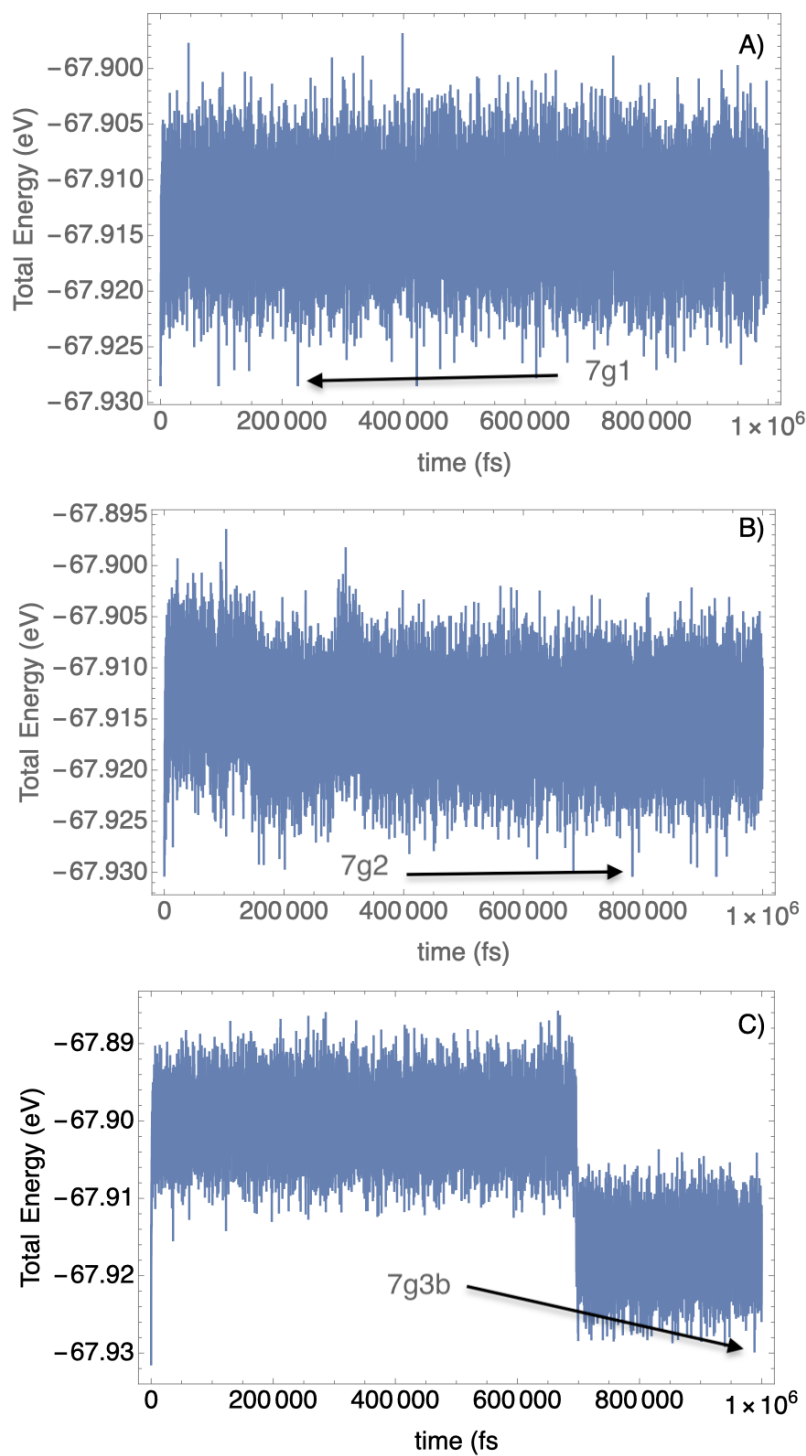


Figure 4.6: Molecular dynamics of  $(TiO_2)_7$  nanoclusters. **A** : 7g1; **B** : 7g2; **C** : 7g3.

4.1. MOLECULAR DYNAMICS SIMULATIONS AND ELECTRONIC STRUCTURE OF  
44  $(TiO_2)_N$ ,  $N = 1 - 10$  CLUSTERS AND ELECTRONIC DISTRIBUTION CALCULATIONS.

Figure 4.7 displays the outcome of the 1ns MD for  $n = 8$  clusters. The MD simulation yields two similar structures (8h3 and 8h4) which have a rapid stabilization period before the actual stabilization to a linear-like structure (Fig.4.7 B-C). In contrast, 8h2 MD presents a complete linear-like structure with no stabilization period as the other two(Fig.4.7 A). Furthermore, note in Table 4.1 that 8h3 and 8h4 structures converge to a single configuration after the relaxation. Also, the major contribution to the HOMO orbitals is given by the O-2p states.

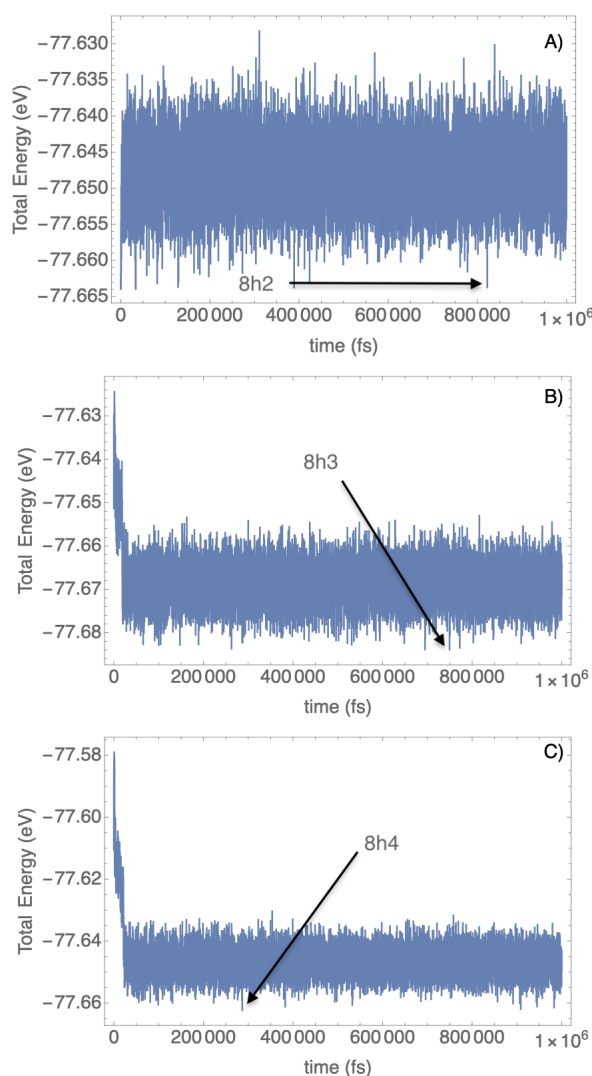


Figure 4.7: Molecular dynamics of  $(TiO_2)_8$  nanoclusters. **A** : 8h2; **B** : 8h3; **C** : 8h4.

Figure 4.8 displays the outcome of the 1ns MD for  $n = 9$  clusters. The 9i1 and 9i2 MD yields linear-like structures with no phase transition present. Nonetheless, in Table 4.1 note that 9i1 and 9i2 structures converge to a single configuration after the relaxation. By consulting Table 4.2 this trend makes sense since  $E_{tot}$  of these structures is around -9000.444 Ha and  $R_g \sim 3.2$ . Furthermore, notice the HOMO orbitals major contributions are given by the O-2p states.

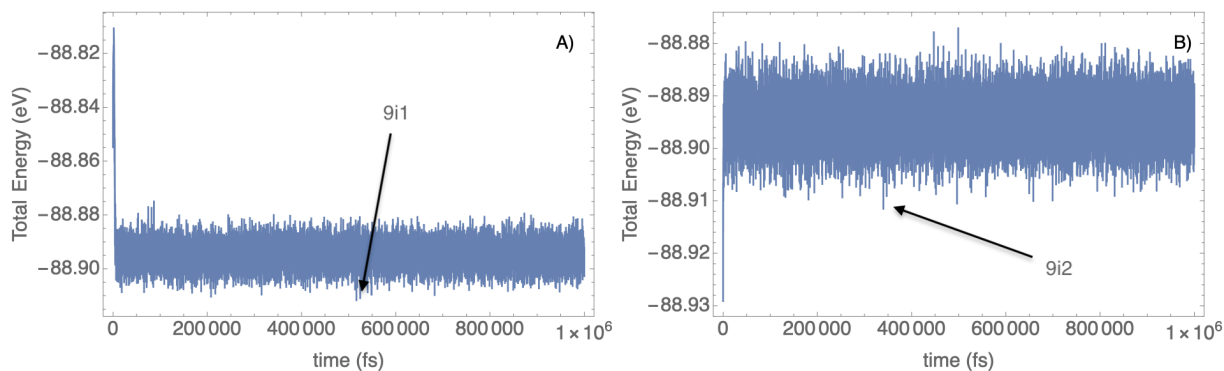


Figure 4.8: Molecular dynamics of  $(TiO_2)_9$  nanoclusters. **A** : 9i1; **B** : 9i2.

Figure 4.9 displays the outcome of the 1 ns MD for  $n = 10$  clusters. First of all, we can notice that for all of the 10j structures exist clear phase transitions. In 10j1 MD (Fig.4.9 A) there are four stair-like structures. In 10j2 MD (Fig.4.9 B) there are two stair-like structures, in particular, this phase transition occurs almost at the end of the MD time. In 10j3 MD (Fig.4.9 C) there are also two stair-like structures, but unlike 10j2, this phase transition occurs at the very beginning of the MD time. Finally, in Table 4.1 it is displayed the HOMO distribution orbitals and are mainly constituted by O-2p states lying in the same plane.

46 4.1. MOLECULAR DYNAMICS SIMULATIONS AND ELECTRONIC STRUCTURE OF  $(TiO_2)_N$ ,  $N = 1 - 10$  CLUSTERS AND ELECTRONIC DISTRIBUTION CALCULATIONS.

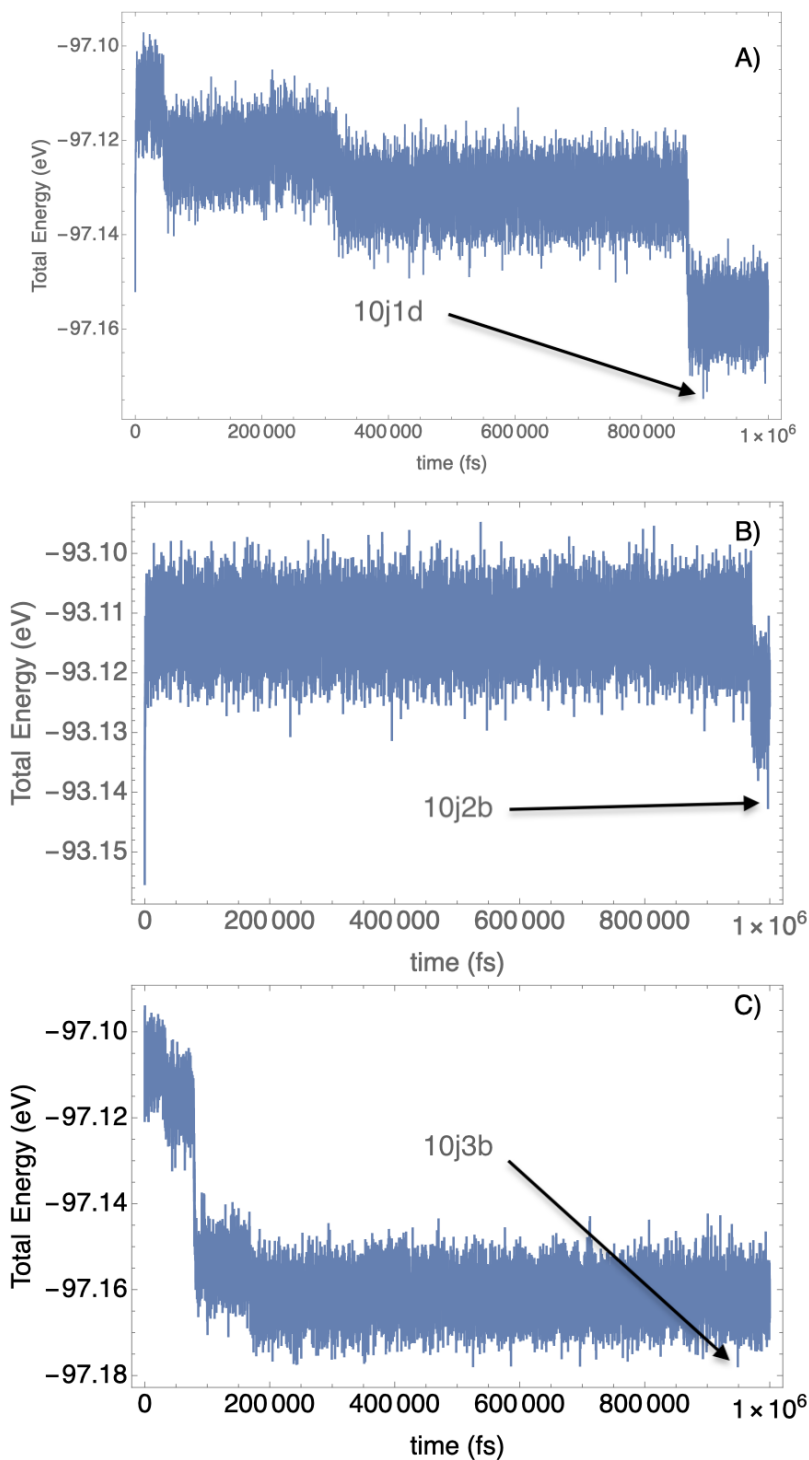
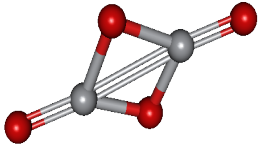
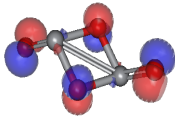
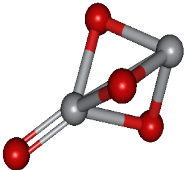
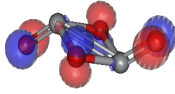
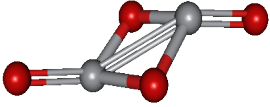
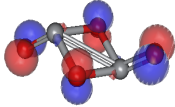


Figure 4.9: Molecular dynamics of  $(TiO_2)_{10}$  nanoclusters. **A** : 10j1; **B** : 10j2; **C** : 10j3.

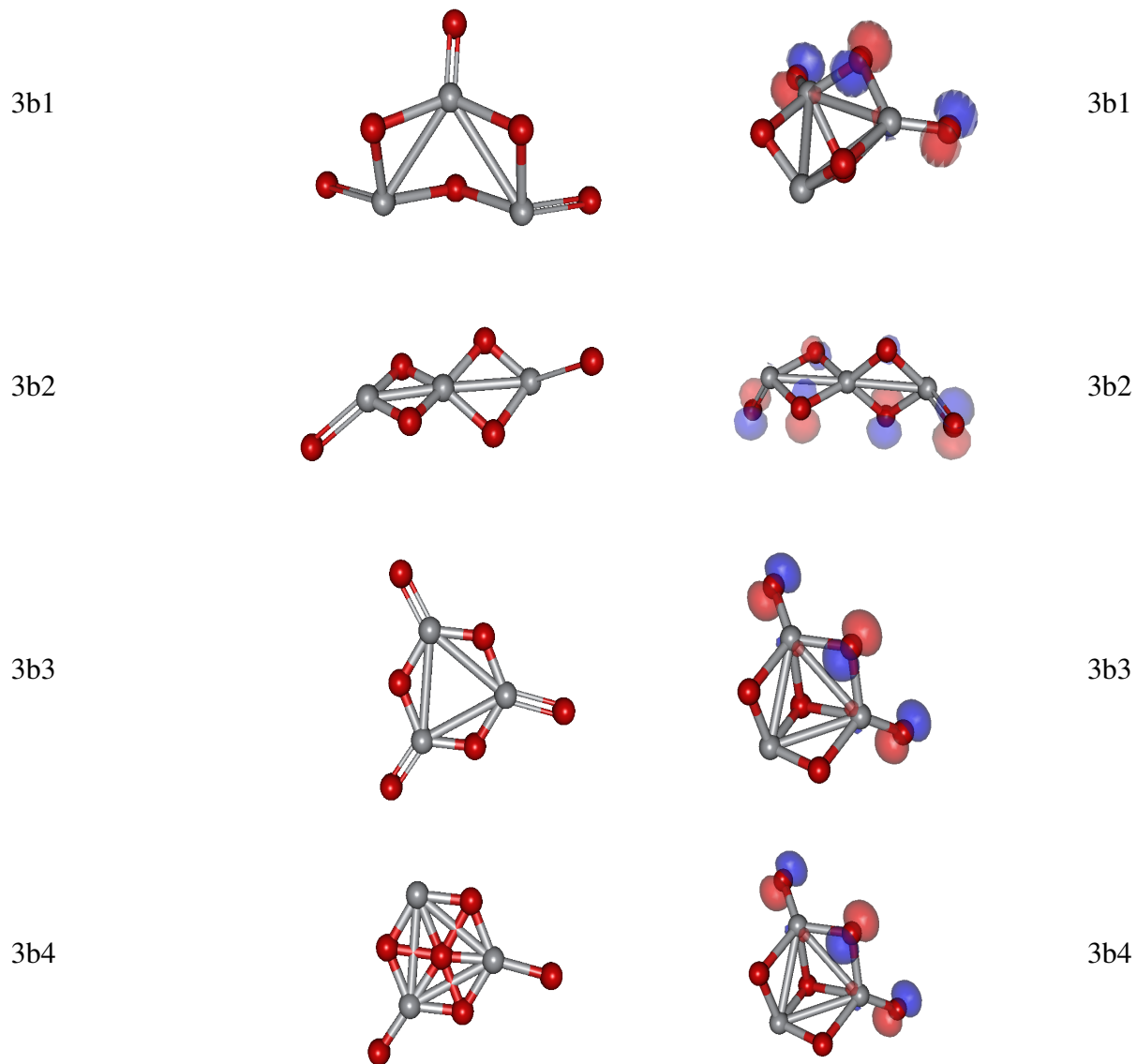
Table.4.1 displays a comparison of each original nanocluster with its corresponding most-stable configuration including the HOMO distributions. As mentioned above, we observe some structures with the same  $n$  to end having similar structures and properties after MD simulations.

Table 4.1: Summary of results, this table displays the initial structure relaxed at 0 K and most stable structure from MD results including the HOMO distribution. The label on the left column corresponds to the structure as labeled in Table 4.2. In all the figures, the isovalue of HOMO was plotted at  $0.06 e/a_0^3$ ; and the O (Ti) atoms are depicted by red (grey) spheres.

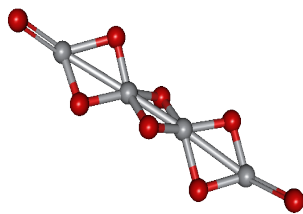
Cluster name	Initial Structure	Most Stable Structure + HOMO	Label
2a1			2a1
2a2			2a2
2a3			2a3

4.1. MOLECULAR DYNAMICS SIMULATIONS AND ELECTRONIC STRUCTURE OF  
48  $(TiO_2)_N$ ,  $N = 1 - 10$  CLUSTERS AND ELECTRONIC DISTRIBUTION CALCULATIONS.

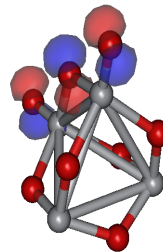
---



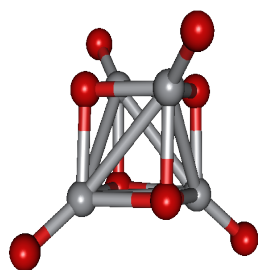
4c1



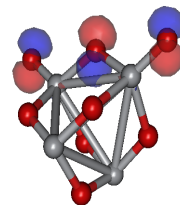
4c1c



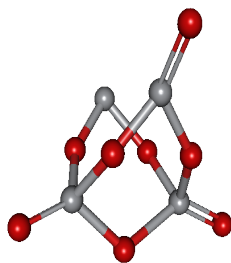
4c2



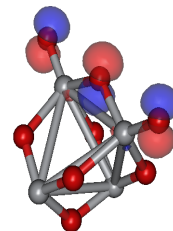
4c2b



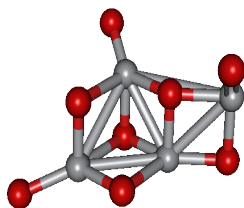
4c3



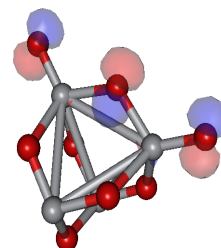
4c3



4c4

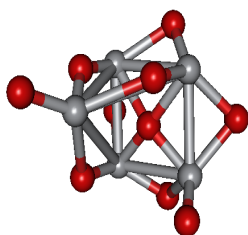


4c4

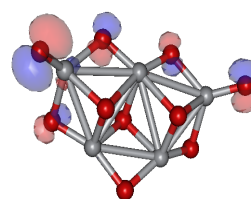


4.1. MOLECULAR DYNAMICS SIMULATIONS AND ELECTRONIC STRUCTURE OF  
50  $(TiO_2)_N$ ,  $N = 1 - 10$  CLUSTERS AND ELECTRONIC DISTRIBUTION CALCULATIONS.

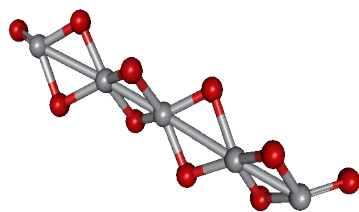
5d1



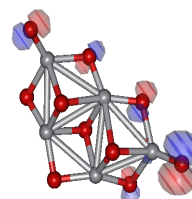
5d1



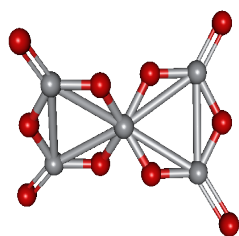
5d2



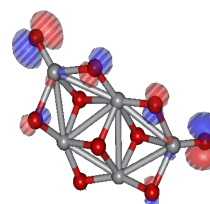
5d2c



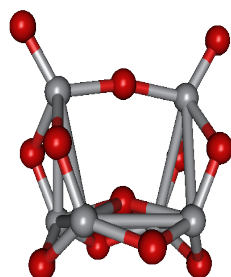
5d3



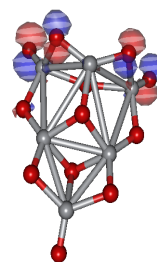
5d3c

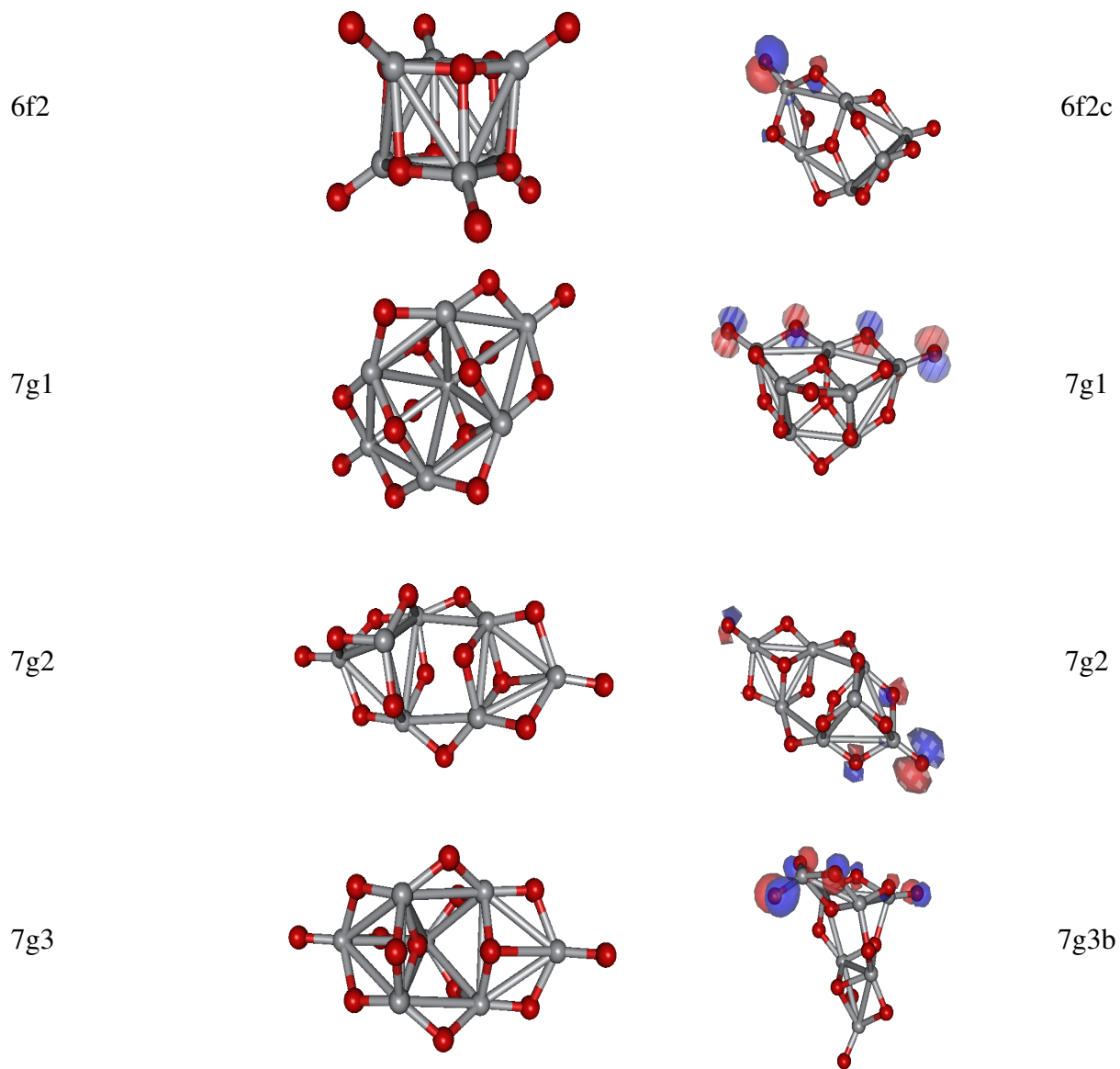


6f1

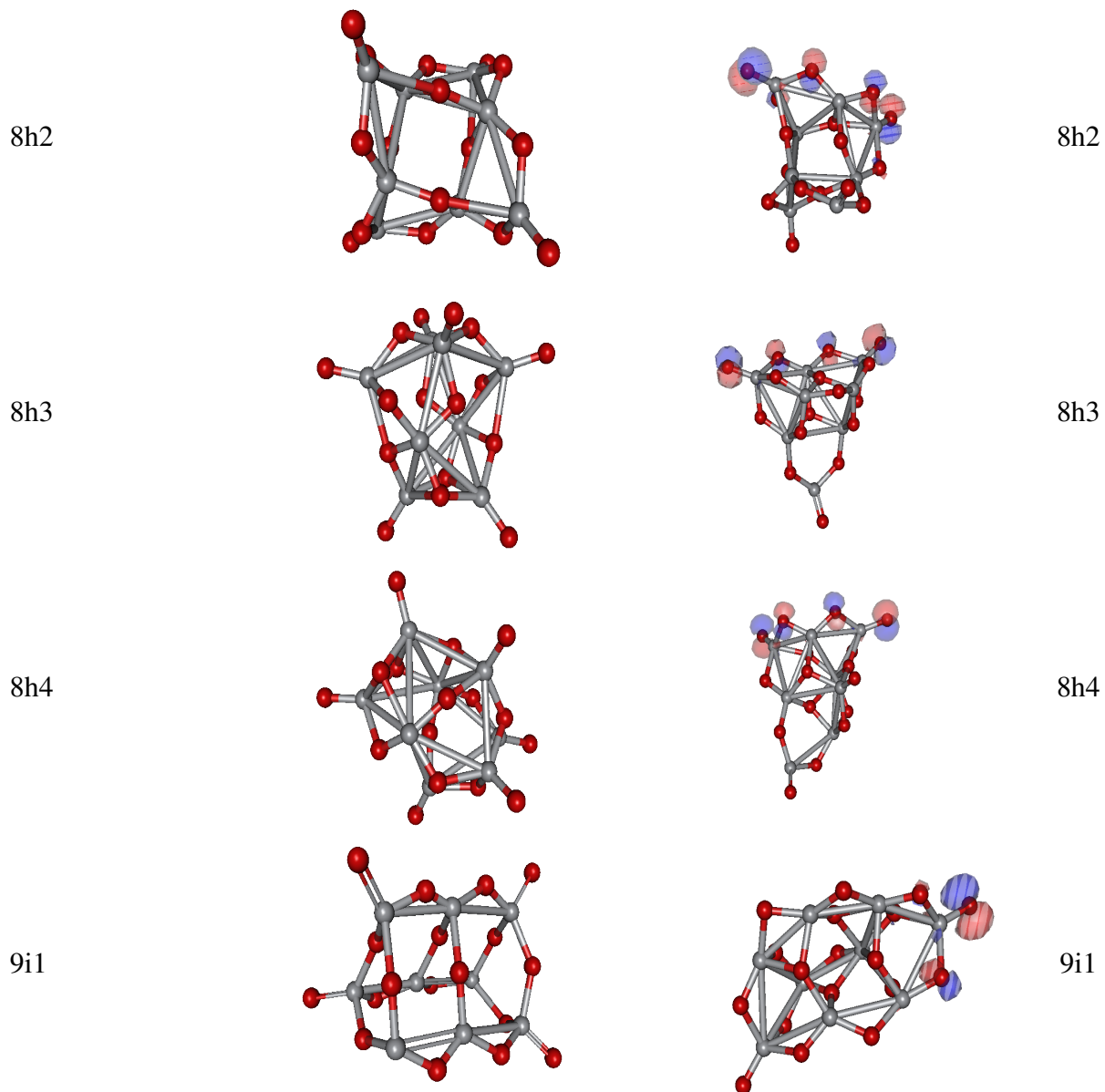


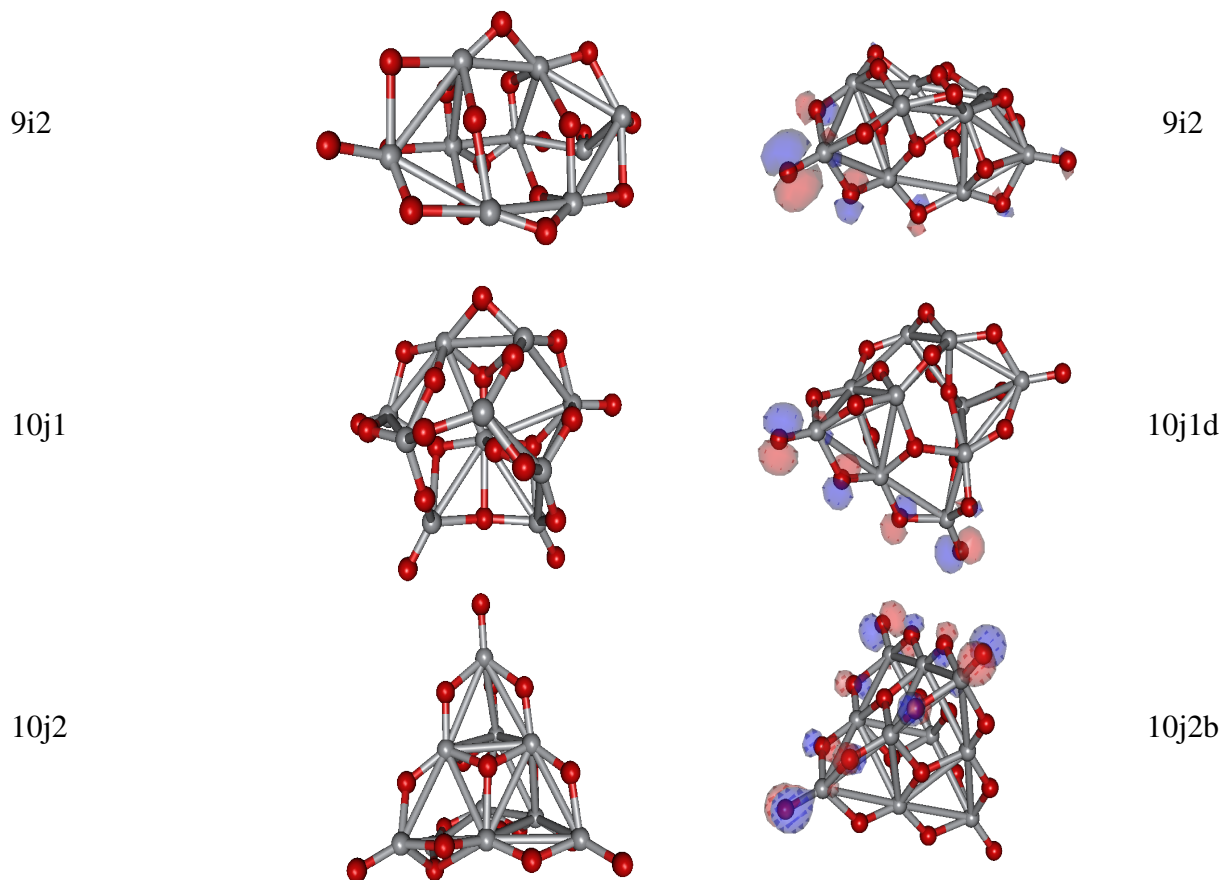
6f1d





4.1. MOLECULAR DYNAMICS SIMULATIONS AND ELECTRONIC STRUCTURE OF  
52  $(TiO_2)_N$ ,  $N = 1 - 10$  CLUSTERS AND ELECTRONIC DISTRIBUTION CALCULATIONS.





## 4.2 Predicted physical properties of the clusters and correlations.

In this section we will introduce the predicted physical properties calculated for each of the clusters.

As we have seen in the previous subsection, MD allows us to compute different phases that come from a single nanocluster originally. In Figure 4.10 it is displayed a summary of all the meta-stable and stable configurations per  $(TiO_2)_n$  nanocluster after MD and posterior *ab initio* relaxation. Above each configuration, it is displayed the corresponding label.

54 4.2. PREDICTED PHYSICAL PROPERTIES OF THE CLUSTERS AND CORRELATIONS.

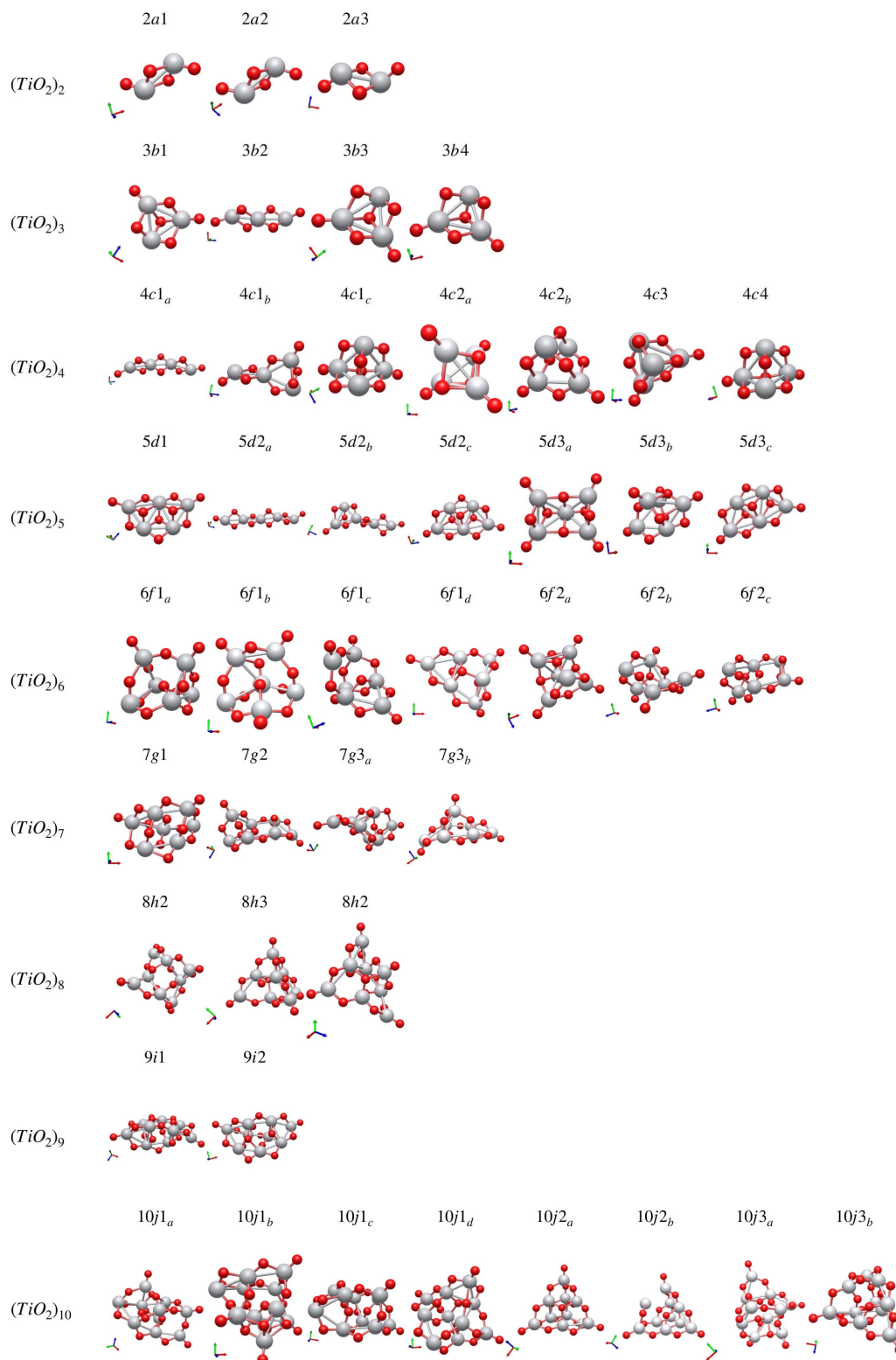


Figure 4.10: Summary of all possible configurations of  $(\text{TiO}_2)_n$  ( $n = 1 - 10$ ) nanoclusters after MD process during 1 ns at room temperature ( $T = 298.15$  K).

Following this, in Table 4.2 they are displayed all the physical properties calculated with ORCA for all the possible configurations found in the MD. These properties are: total energy( $E_{tot}$ ) in Ha, dipole moment( $D$ ) in a.u., quadrupole moment ( $Q$ ) in a.u., isotropic polarizability ( $P$ ) in a.u., electronic Energy ( $E_{elec}$ ) in Ha, nuclear repulsion ( $E_{NR}$ ) in Ha, HOMO energy in Ha, LUMO energy in Ha, energy gap ( $E_g$ ) in Ha, zero-point energy ( $E_{ZP}$ ) in Ha and Gyration radius ( $R_g$ ) in Å.

Table 4.2: DFT-B3LYP computed results: total Energy( $E_{tot}$ ), dipole moment( $p$ ), quadrupole moment ( $Q$ ), isotropic polarizability ( $P$ ), electronic Energy ( $E_{elec}$ ), nuclear repulsion ( $E_{NR}$ ), HOMO, LUMO, energy gap ( $E_g$ ), zero-point energy ( $E_{ZP}$ ) and Gyration radius ( $R_g$ ). In this table,  $p$ ,  $Q$  and  $\alpha$  is given in a.u., the energies in Eh and  $R_g$  in Å.

Syst	$E_{tot}$	D	Q	P	$E_{elec}$	$E_{NR}$	HOMO	LUMO	$E_g$	$E_{ZP}$	$R_g$
2a1	-1999.951	0.002	-40.985	66.537	-2524.296	524.331	-0.296	-0.113	0.183	0.014	1.66
2a2	-1999.951	0.008	-40.947	66.448	-2524.69	524.724	-0.296	-0.112	0.183	0.014	1.655
2a3	-1999.951	0.001	-40.959	66.583	-2524.186	524.22	-0.295	-0.113	0.183	0.014	1.64
3b1	-3000.018	3.623	-62.364	97.631	-4150.931	1150.89	-0.288	-0.152	0.136	0.023	1.922
3b2	-3000.004	2.397	-58.857	106.151	-4064.775	1064.748	-0.297	-0.119	0.178	0.022	2.406
3b3	-3000.018	3.55	-62.426	97.688	-4151.434	1151.393	-0.287	-0.153	0.134	0.023	1.908
3b4	-3000.018	3.55	-62.374	97.644	-4151.659	1151.618	-0.287	-0.153	0.134	0.023	1.909
4c1a	-4000.06	0.223	-78.311	150.9	-5696.359	1696.269	-0.306	-0.124	0.182	0.031	3.104
4c1b	-4000.062	1.328	-80.563	140.896	-5789.366	1789.274	-0.297	-0.139	0.158	0.031	2.595
4c1c	-4000.078	4.813	-80.943	131.037	-5900.363	1900.255	-0.267	-0.154	0.112	0.03	2.117
4c2a	-4000.048	0.245	-90.043	132.91	-5947.72	1947.642	-0.343	-0.18	0.163	0.03	2.229
4c2b	-4000.078	4.844	-80.944	131	-5901.009	1900.901	-0.266	-0.155	0.112	0.031	2.238
4c3	-4000.078	4.863	-62.374	130.883	-5901.033	1900.924	-0.267	-0.154	0.112	0.031	2.126
4c4	-4000.078	4.842	-80.833	130.622	-5903.319	1903.211	-0.266	-0.154	0.112	0.031	2.135
5d1	-5000.156	1.622	-108.322	171.808	-7838.208	2838.012	-0.319	-0.142	0.177	0.039	2.606
5d2a	-5000.115	2.373	-97.819	198.023	-7400.023	2399.869	-0.309	-0.127	0.182	0.039	3.897
5d2b	-5000.116	3.487	-96.023	184.965	-7511.012	2510.857	-0.298	-0.141	0.157	0.039	3.308
5d2c	-5000.157	1.655	-108.329	171.858	-7838.032	2837.836	-0.32	-0.143	0.177	0.039	2.615
5d3a	-5000.102	0.952	-115.34	169.615	-7766.247	2766.107	-0.318	-0.173	0.145	0.038	2.588
5d3b	-5000.106	1.152	-110.491	167.727	-7875.347	2875.203	-0.333	-0.164	0.169	0.038	2.395
5d3c	-5000.157	1.581	-108.286	171.666	-7839.045	2838.849	-0.32	-0.142	0.178	0.039	2.612
6f1a	-6000.236	4.692	-125.531	196.583	-9944.508	3944.225	-0.274	-0.153	0.121	0.047	2.703
6f1b	-6000.202	4.184	-127.708	198.685	-9885.53	3885.281	-0.286	-0.159	0.127	0.047	2.746
6f1c	-6000.263	2.416	-127.675	198.915	-9972.019	3971.707	-0.318	-0.146	0.171	0.048	2.867

56 4.2. PREDICTED PHYSICAL PROPERTIES OF THE CLUSTERS AND CORRELATIONS.

6f1d	-6000.221	2.265	-134.087	207.213	-9813.578	3813.31	-0.327	-0.161	0.166	0.047	2.97
6f2a	-6000.189	4.113	-132.015	197.262	-9943.749	3943.514	-0.325	-0.192	0.133	0.047	2.679
6f2b	-6000.187	3.104	-129.567	202.832	-9832.189	3831.956	-0.298	-0.168	0.13	0.046	2.808
6f2c	-6000.236	4.381	-125.035	204.268	-9813.972	3813.689	-0.302	-0.165	0.138	0.047	2.832
7g1	-7000.313	2.953	-150.672	239.193	-12152.857	5152.489	-0.311	-0.146	0.165	0.055	2.846
7g2	-7000.308	2.308	-147.425	241.865	-11909.032	4908.669	-0.31	-0.163	0.148	0.055	3.202
7g3	-7000.339	0.944	-149.608	236.466	-12136.623	5136.227	-0.321	-0.14	0.181	0.056	3.002
7g3b	-7000.31	0.494	-150.362	238.767	-12015.293	5014.927	-0.321	-0.157	0.164	0.056	3.102
8h2	-8000.347	1.923	-174.325	279.869	-14272.981	6272.571	-0.326	-0.153	0.172	0.062	3.27
8h3	-8000.392	1.975	-174.107	283.123	-14261.86	6261.405	-0.315	-0.149	0.166	0.063	3.121
8h4	-8000.345	2.72	-174.231	278.413	-14329.248	6328.84	-0.323	-0.153	0.17	0.063	3.254
9i1	-9000.444	1.488	-195.741	311.845	-16920.518	7920.002	-0.319	-0.15	0.169	0.072	3.206
9i2	-9000.44	1.725	-195.527	307.151	-16972.994	7972.483	-0.324	-0.149	0.174	0.072	3.211
10j1a	-10000.497	5.014	-217.14	348.488	-19180.405	9179.829	-0.297	-0.164	0.133	0.079	3.462
10j1b	-10000.484	5.512	-212.922	333.269	-19630.357	9629.794	-0.315	-0.173	0.142	0.079	3.21
10j1c	-10000.561	5.185	-211.581	338.88	-19412.476	9411.834	-0.304	-0.156	0.148	0.081	3.307
10j1d	-10000.526	4.704	-218.502	345.46	-19293.608	9293.002	-0.309	-0.186	0.123	0.08	3.414
10j2a	-10000.572	0.061	-229.921	351.681	-19262.094	9261.443	-0.338	-0.166	0.171	0.079	3.362
10j2b	-10000.572	0.065	-229.937	351.682	-19262.256	9261.605	-0.338	-0.166	0.171	0.079	3.416
10j3a	-10000.501	2.59	-220.999	342.615	-19501.178	9500.598	-0.329	-0.165	0.165	0.08	3.317
10j3b	-10000.522	4.526	-215.514	348.665	-19249.656	9249.055	-0.308	-0.176	0.132	0.079	3.363

Figure 4.11, which displays a summary of the likely correlations that might appear on the whole set of data presented in Table 4.2. Our main goal is to provide trends considering the size of the  $(\text{TiO}_2)_n$  clusters described by  $R_g$  with the computed values. After applying statistical analysis; we notice that  $R_g$  shows correlations above absolute 0.7 with  $E_{tot}$ ,  $Q$ ,  $\alpha$ ,  $E_{elec}$ ,  $E_{NR}$  and the  $E_{ZP}$ .

Furthermore, making use of this data we can explore the size-dependence of the physical properties of the clusters, that in our case is expressed by the gyration ratio. Polynomial trends were found for the following properties: electronic energy  $E_{elec}$  (Fig. 6.2), isotropic polarizability  $P$  (Fig. 6.3), nuclear repulsion  $E_{NR}$  (Fig. 6.4), quadrupole moment  $Q$  (Fig. 6.5), total energy  $E_{tot}$  (Fig. 6.1) and zero-point energy  $E_{ZP}$  (Fig. 6.6). The polynomial trends with their respective  $R^2$  are displayed in the appendix A section.

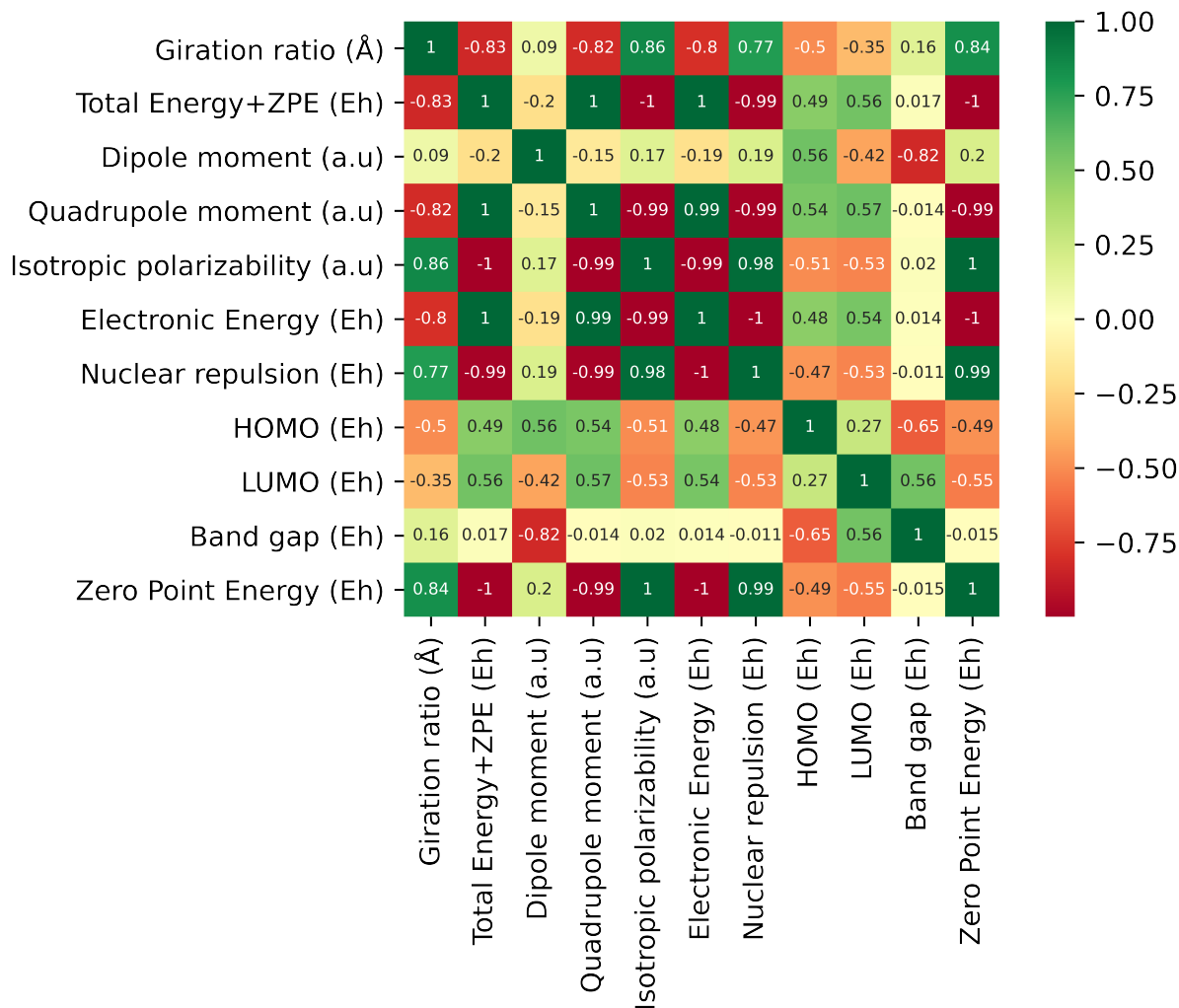


Figure 4.11: Correlation matrix which relates the different physical-chemical properties predicted by B3LYP electronic structure calculations. Mind that the values presented here means that 1 (-1) indicates a perfectly positive (negative) linear correlation between two variables while 0 value indicates no correlation between variables.

### 4.3 Stability of the clusters: Magic clusters.

In general, the total energy is not enough in order to determine the stability and abundance of the clusters, specially when we want to establish an analysis depending on their size. We find a solution for this exploiting the idea of the so-called magic clusters. Experimentally, the formation of clusters is an stochastic process that yields systems of different number of atoms. Depending on the size, some clusters might have increased stability resulting in the formation of more clusters of that specific size compared with other sizes<sup>53</sup>. We classify a cluster as magic if a pair of such clusters is stable against the transfer of one atom between them. Then, stability can be determined with respect to closest neighbour clusters through a second order numerical derivative, such that if it is positive (negative) the cluster is magic (not magic) as stated below<sup>54</sup>:

$$\Delta^2 E = E(n + 1) + E(n - 1) - 2E(n) > 0 \quad (4.1)$$

Then, we took the most stable configuration per number of  $(\text{TiO}_2)_n$  molecules and applied the stability criterion obtaining that clusters with  $n = 3, 6, 7, 8$  are predicted the most stable and abundant as we can see in Figure 4.12. The thick blue line and red dots represent the stability of the cluster based on the total energy including  $E_{ZP}$ . Meanwhile, the gray dashed line and black points represent the stability criterion based on the total energy without  $E_{ZP}$ .

Comparing these two cases allows us to analyze the role of the zero-point energy  $E_{ZP}$  on the cluster stability. In principle,  $E_{ZP}$  comes from the Heisenberg uncertainty which states that quantum systems fluctuate even at their lowest energy state, such that we get fundamental vibrations even at 0 K. At first instance, we could think that adding  $E_{ZP}$  would stabilize the clusters due to  $E_{ZP}$  is always positive, but in fact, this does not hold for all structures as we see in Figure 4.12 where the total energy (red dot) is below the total energy without  $E_{ZP}$  (black dot) for  $n = 3, 7, 9$ . An special case is portrayed in cluster  $(\text{TiO}_2)_8$ , which is unstable when  $E_{ZP}$  is not considered ( $\Delta^2 E < 0$ ), but it becomes stable as we add this contribution ( $\Delta^2 E > 0$ ). Then, including  $E_{ZP}$  or vibrational effects allow us to have more accurate prediction of the stability and abundance.

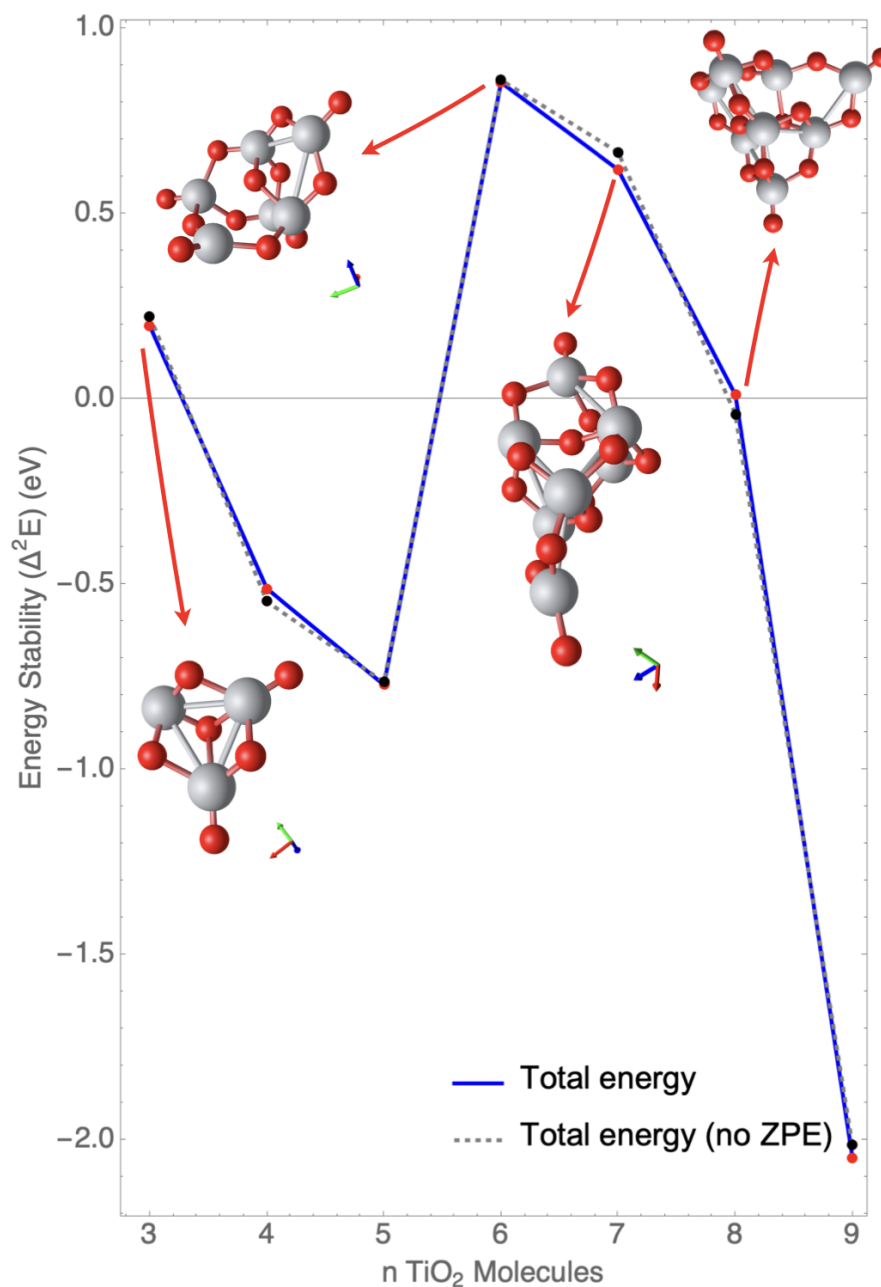


Figure 4.12: Energy stability ( $\Delta^2 E$ ) with respect to the number of  $(\text{TiO}_2)_n$  molecules. The blue thick line and red points represents the energy stability computed with all contributions, whereas the gray dashed line and black points represents the energy stability excluding the  $E_{ZP}$ . Notice the predicted magic clusters ( $\Delta^2 E > 0$ ) are  $(\text{TiO}_2)_n$  with  $n = 3, 6, 7, 8$ .



# Chapter 5

## Conclusions & Outlook

In this thesis we have described the electronic and atomic of  $(\text{TiO}_2)_n$  nanoclusters in different configurations ( $n = 1-10$ ). First, we constructed all the different configurations of the nanoclusters using the ASE software. Then we performed an initial relaxation to each of the nanoclusters with the semi-empirical GFNn-xTB package, obtaining already different dispositions in some of the clusters. Next, we performed molecular dynamics for 1 ns at room temperature ( $T = 278.15$  K) using the GFNn-xTB package to detect all the possible meta- stable configurations of each of the nanoclusters. In general, most of the nanoclusters presented at least one phase transition during the molecular dynamic process, such that we obtained from 2 to 4 topologically different configurations for each cluster. Following, we performed an all-electron ab initio DFT relaxation at 0 K on all the meta-stable and most-stable configurations detected in the molecular dynamics. This was done in ORCA package implementing the B3LYP hybrid functional. Finally, we calculate the electronic structure, total energy ( $E_{tot}$ ), dipole moment ( $P$ ), quadrupole moment ( $Q$ ), isotropic polarizability ( $\alpha$ ), electronic energy ( $E_{elec}$ ), nuclear repulsion ( $E_{NR}$ ), HOMO, LUMO, energy gap ( $E_g$ ), zero-point energy ( $E_{ZP}$ ) and gyration radius ( $R_g$ ) of each of the relaxed nanoclusters. Systematic analysis of the computed structures shows similarities in some cases; the HOMO is observed to have O-2p character mainly. Statistical analysis of the computed physical-chemical properties shows an important correlation of the characteristic size of the cluster represented by  $R_g$  with  $E_{tot}$ ,  $Q$ ,  $\alpha$ ,  $E_{elec}$ ,  $E_{NR}$  and the  $E_{ZP}$ .

Further analysis on the stability of the clusters based on size-dependant criterion ( $\Delta^2 E$ ) determine the magic clusters, the most stable-abundant in nature. Furthermore, we portraint the

role of the  $E_{ZP}$  in the stability of the clusters as they present a subtle yet appreciable difference in their behavior when  $E_{ZP}$  is considered in the calculations. Finally, these results are a relevant contribution towards the understanding of the size-induced properties of  $\text{TiO}_2$  nanoclusters for the future design of nanoparticles with desired features.

Even though some  $(\text{TiO}_2)_n$  clusters properties have been already studied theoretically thorough DFT simulations<sup>55,56</sup>, using the B3LYP hybrid functional<sup>14,15</sup>, it is important to stress that those studies developed their calculations inside the zero-point temperature frame, in other words, the configurations presented are stable close to 0 K, but that does not guaranty they are present in nature, since they may or may not be stable at higher temperatures. In contrast, we performed the MD simulation which feature is to find stable and meta-stable configurations at room temperature, as we have seen in the change of phases during the MD time. Incorporating this method as a previous step to the full-relaxation with B3LYP give us a wider and more detailed spectrum, since we can find not only the global zero-point structure, but more possible stable structures that might be formed in experiments.

Finally, it is worth mentioning that the molecular modelling in this work was prepared in agreement with European Materials Modelling Council (EMMC) document that describe the standard modelling scheme, i.e., flowchart for materials modelling. The physical-based and data-based models implemented for the computation and analysis of the results were developed according to the recommendations by EMMC as a preliminary result for design of safer and more efficient  $\text{TiO}_2$  based photocatalysts in the line with safety and sustainability-by-design strategy.

# Chapter 6

## Appendix A

### 6.1 Size-Dependence of physical properties in clusters.

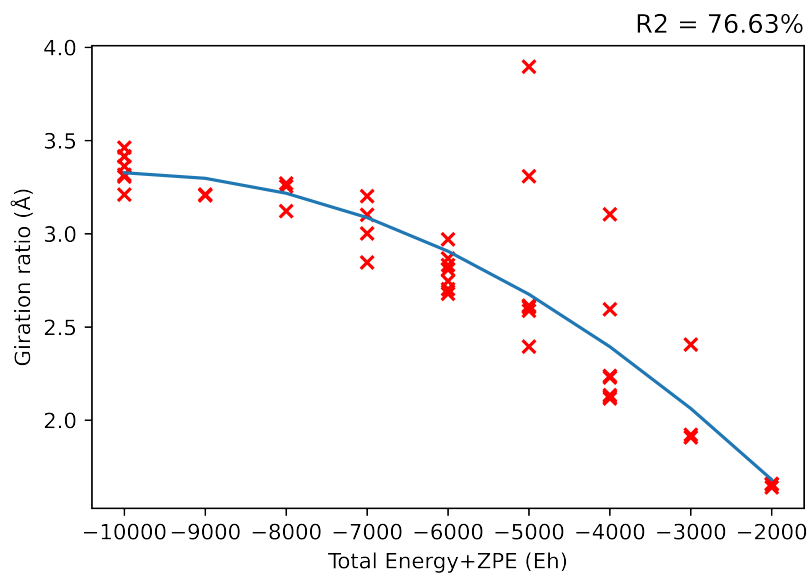


Figure 6.1: Size-dependence of the total energy ( $E_{tot}$ ) of the clusters with the gyration ratio ( $R_g$ ). Notice we get a polynomial relation with  $R^2 = 76.63\%$

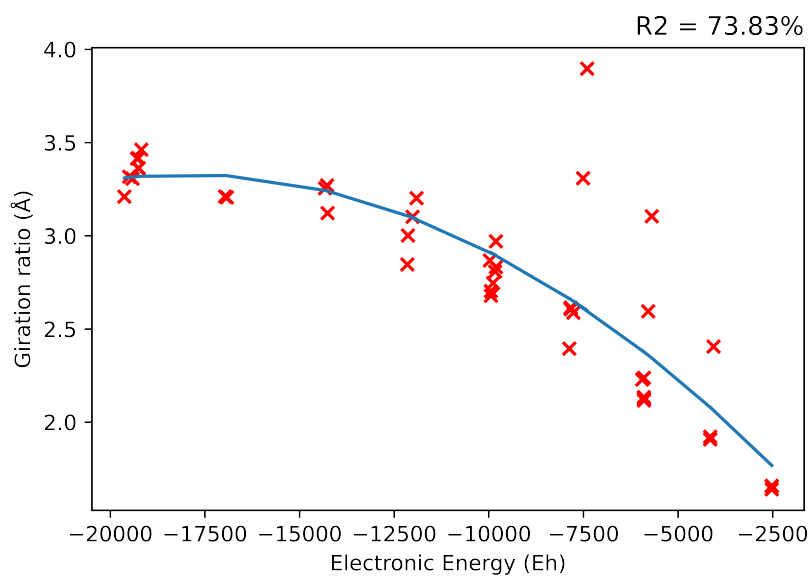


Figure 6.2: Size-dependence of the electronic energy ( $E_{tot}$ ) of the clusters with the gyration ratio ( $R_g$ ). Notice we get a polynomial relation with  $R^2 = 73.83\%$

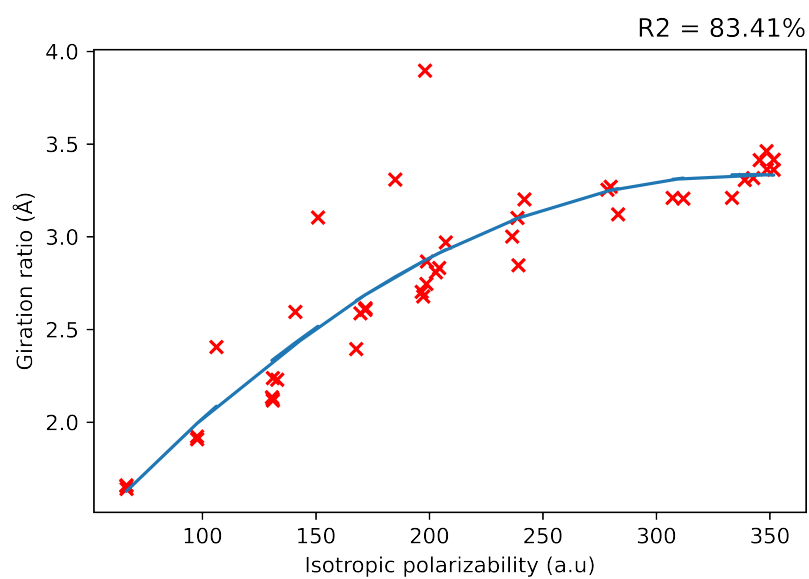


Figure 6.3: Size-dependence of the isotropic polarizability ( $P$ ) of the clusters with the gyration ratio ( $R_g$ ). Notice we get a polynomial relation with  $R^2 = 83.41\%$

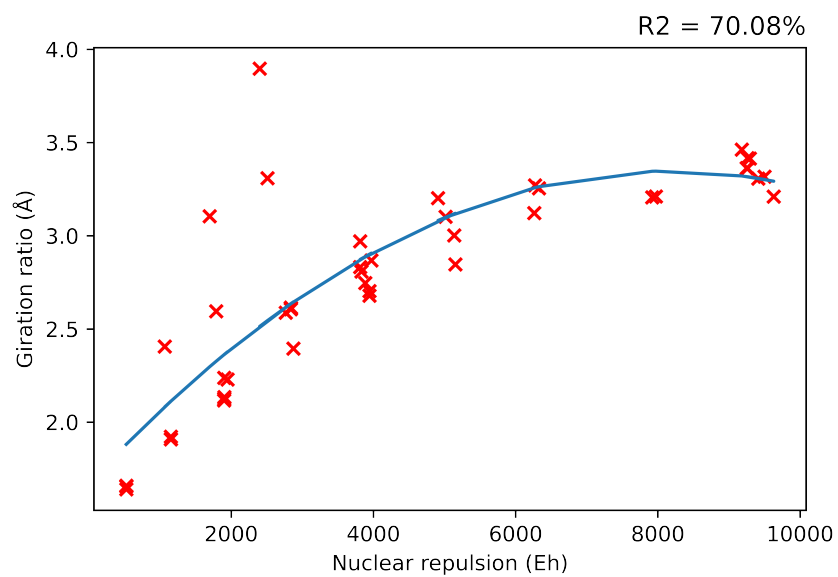


Figure 6.4: Size-dependence of the nuclear repulsion ( $E_{NR}$ ) of the clusters with the gyration ratio ( $R_g$ ). Notice we get a polynomial relation with  $R^2 = 70.08\%$

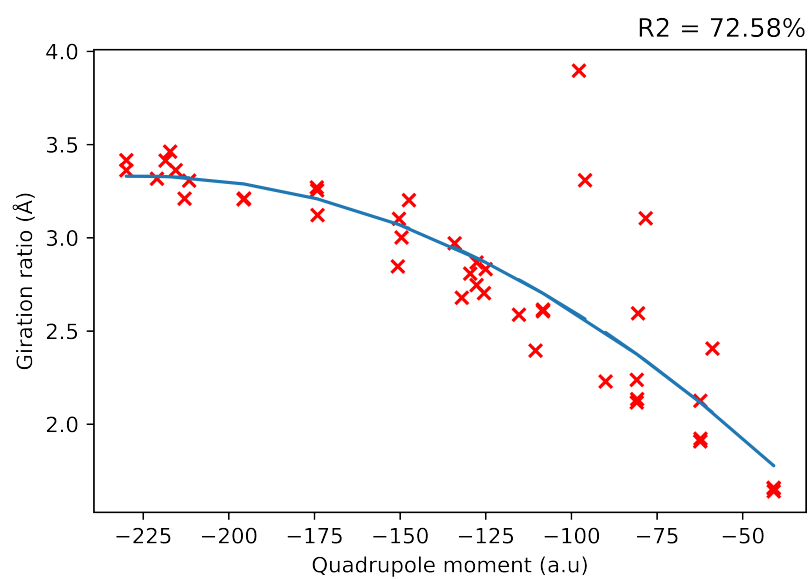


Figure 6.5: Size-dependence of the quadrupole moment ( $Q$ ) of the clusters with the gyration ratio ( $R_g$ ). Notice we get a polynomial relation with  $R^2 = 72.58\%$

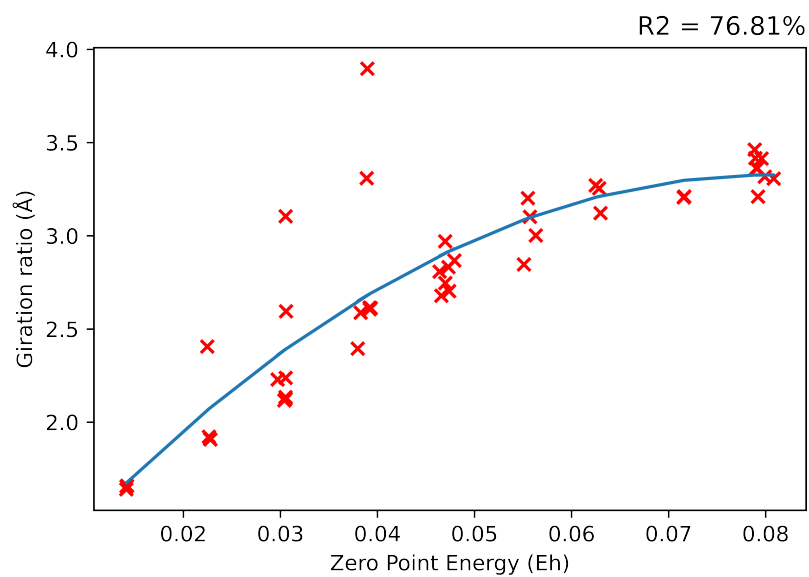


Figure 6.6: Size-dependence of the zero-point energy ( $E_{ZP}$ ) of the clusters with the gyration ratio ( $R_g$ ). Notice we get a polynomial relation with  $R^2 = 76.81\%$

# Bibliography

- [1] Schneider, J.; Matsuoka, M.; Takeuchi, M.; Zhang, J.; Horiuchi, Y.; Anpo, M.; Bahnemann, D. W. Understanding TiO<sub>2</sub> Photocatalysis: Mechanisms and Materials. *Chemical Reviews* **2014**, *114*, 9919–9986.
- [2] Bai, J.; Zhou, B. Titanium Dioxide Nanomaterials for Sensor Applications. *Chemical Reviews* **2014**, *114*, 10131–10176.
- [3] Angelis, F. D.; Valentin, C. D.; Fantacci, S.; Vittadini, A.; Selloni, A. Theoretical Studies on Anatase and Less Common TiO<sub>2</sub> Phases: Bulk, Surfaces, and Nanomaterials. *Chemical Reviews* **2014**, *114*, 9708–9753.
- [4] Catlow, C. R. A.; Bromley, S. T.; Hamad, S.; Mora-Fonz, M.; Sokol, A. A.; Woodley, S. M. Modelling nano-clusters and nucleation. *Phys. Chem. Chem. Phys.* **2010**, *12*, 786–811.
- [5] Bannwarth, C.; Caldeweyher, E.; Ehlert, S.; Hansen, A.; Pracht, P.; Seibert, J.; Spicher, S.; Grimme, S. Extended tight-binding quantum chemistry methods. *WIREs Computational Molecular Science* **2020**, *11*.
- [6] Neese, F. The ORCA program system. *WIREs Computational Molecular Science* **2011**, *2*, 73–78.
- [7] Gogotsi, Y. *Nanomaterials handbook*; CRC Press: Boca Raton, 2017.
- [8] Goldbeck, G.; Court, C. *The Economic Impact Of Materials Modelling*. 2016,
- [9] Payne, M. *Handbook of Materials Modeling*; Springer International Publishing, 2020; pp 21–28.

- [10] Noorden, R. V.; Maher, B.; Nuzzo, R. The top 100 papers. *Nature* **2014**, *514*, 550–553.
- [11] Zangwill, A. The education of Walter Kohn and the creation of density functional theory. *Archive for History of Exact Sciences* **2014**, *68*, 775–848.
- [12] Bai, Y.; Mora-Seró, I.; Angelis, F. D.; Bisquert, J.; Wang, P. Titanium Dioxide Nanomaterials for Photovoltaic Applications. *Chemical Reviews* **2014**, *114*, 10095–10130.
- [13] Rajh, T.; Dimitrijevic, N. M.; Bissonnette, M.; Koritarov, T.; Konda, V. Titanium Dioxide in the Service of the Biomedical Revolution. *Chemical Reviews* **2014**, *114*, 10177–10216.
- [14] Oprea, C.; Gîrțu, M. Structure and Electronic Properties of TiO<sub>2</sub> Nanoclusters and Dye–Nanocluster Systems Appropriate to Model Hybrid Photovoltaic or Photocatalytic Applications. *Nanomaterials* **2019**, *9*, 357.
- [15] Arab, A.; Ziari, F.; Fazli, M. Electronic structure and reactivity of (TiO<sub>2</sub>) (n= 1–10) nanoclusters: Global and local hardness based DFT study. *Computational Materials Science* **2016**, *117*, 90–97.
- [16] Oprea, C. I.; Panait, P.; AbdelAal, R. M.; Cirtu, M. A. DFT Calculations of Structure and Optical Properties in Wide Band-Gap Semiconductor Clusters for Dye-Sensitized Solar Cells. 2018; <https://doi.org/10.1109/smicnd.2018.8539813>.
- [17] wang Qu, Z.; Kroes, G.-J. Theoretical Study of Stable, Defect-Free (TiO<sub>2</sub>)<sub>n</sub> Nanoparticles with n = 10-16. *The Journal of Physical Chemistry C* **2007**, *111*, 16808–16817.
- [18] Giustino, F. *Materials modelling using density functional theory: properties and predictions*; Oxford University Press, 2014.
- [19] Sholl, D. *Density functional theory : a practical introduction*; Wiley: Hoboken, N.J, 2009.
- [20] Patterson, J. D.; Bailey, B. C. *Solid-State Physics: introduction to the theory*; Springer International Publishing, 2018.
- [21] Groß, A. *Theoretical Surface Science*; Springer Berlin Heidelberg, 2003.

- [22] Mardirossian, N.; Head-Gordon, M. Thirty years of density functional theory in computational chemistry: an overview and extensive assessment of 200 density functionals. 2017, *115*, 2315–2372.
- [23] *Mathematical Physics in Theoretical Chemistry*; Elsevier, 2019.
- [24] Perdew, J. P. Jacob's ladder of density functional approximations for the exchange-correlation energy. 2001; <https://doi.org/10.1063/1.1390175>.
- [25] Kohn, W.; Sham, L. J. Self-Consistent Equations Including Exchange and Correlation Effects. 1965, *140*, A1133–A1138.
- [26] Perdew, J. P.; Ruzsinszky, A.; Tao, J.; Staroverov, V. N.; Scuseria, G. E.; Csonka, G. I. Prescription for the design and selection of density functional approximations: More constraint satisfaction with fewer fits. 2005, *123*, 062201.
- [27] Fiolhais, C., Nogueira, F., Marques, M. A. L., Eds. *A Primer in Density Functional Theory*; Springer Berlin Heidelberg, 2003.
- [28] Perdew, J. P.; Yue, W. Accurate and simple density functional for the electronic exchange energy: Generalized gradient approximation. 1986, *33*, 8800–8802.
- [29] Perdew, J. P.; Burke, K.; Wang, Y. Generalized gradient approximation for the exchange-correlation hole of a many-electron system. 1996, *54*, 16533–16539.
- [30] Hammer, B.; Hansen, L. B.; Nørskov, J. K. Improved adsorption energetics within density-functional theory using revised Perdew-Burke-Ernzerhof functionals. 1999, *59*, 7413–7421.
- [31] Becke, A. D. Density-functional exchange-energy approximation with correct asymptotic behavior. 1988, *38*, 3098–3100.
- [32] Becke, A. D.; Roussel, M. R. Exchange holes in inhomogeneous systems: A coordinate-space model. 1989, *39*, 3761–3767.
- [33] Becke, A. D. Exploring the limits of gradient corrections in density functional theory. 1999, *20*, 63–69.

- [34] Becke, A. D. Hartree-Fock exchange energy of an inhomogeneous electron gas. 1983, *23*, 1915–1922.
- [35] Becke, A. D. A new inhomogeneity parameter in density-functional theory. 1998, *109*, 2092–2098.
- [36] Becke, A. D. A new mixing of Hartree–Fock and local density-functional theories. 1993, *98*, 1372–1377.
- [37] Becke, A. D. Density-functional thermochemistry. III. The role of exact exchange. 1993, *98*, 5648–5652.
- [38] Becke, A. D. Density-functional exchange-energy approximation with correct asymptotic behavior. 1988, *38*, 3098–3100.
- [39] Lee, C.; Yang, W.; Parr, R. G. Development of the Colle-Salvetti correlation-energy formula into a functional of the electron density. 1988, *37*, 785–789.
- [40] Vosko, S. H.; Wilk, L.; Nusair, M. Accurate spin-dependent electron liquid correlation energies for local spin density calculations: a critical analysis. 1980, *58*, 1200–1211.
- [41] Jensen, F. *Introduction to Computational Chemistry*; John Wiley & Sons, Incorporated: Somerset, 2016.
- [42] Parrill, A. *Reviews in computational chemistry*; Wiley: Hoboken, 2016.
- [43] Helgaker, T. *Molecular electronic-structure theory*; Wiley: Chichester New York, 2000.
- [44] Zaleśny, R. *Linear-scaling techniques in computational chemistry and physics : methods and applications*; Springer: Dordrecht London, 2011.
- [45] Neese, F. An improvement of the resolution of the identity approximation for the formation of the Coulomb matrix. 2003, *24*, 1740–1747.
- [46] Neese, F.; Wennmohs, F.; Hansen, A.; Becker, U. Efficient, approximate and parallel Hartree–Fock and hybrid DFT calculations. A ‘chain-of-spheres’ algorithm for the Hartree–Fock exchange. 2009, *356*, 98–109.

- [47] Bannwarth, C.; Caldeweyher, E.; Ehlert, S.; Hansen, A.; Pracht, P.; Seibert, J.; Spicher, S.; Grimme, S. Extended tight-binding quantum chemistry methods. 2020, *11*.
- [48] Brázdová, V. *Atomistic computer simulations : a practical guide*; Wiley-VCH: Weinheim, 2013.
- [49] Bannwarth, C.; Ehlert, S.; Grimme, S. GFN2-xTB—An Accurate and Broadly Parametrized Self-Consistent Tight-Binding Quantum Chemical Method with Multipole Electrostatics and Density-Dependent Dispersion Contributions. 2019, *15*, 1652–1671.
- [50] Hehre, W. J.; Stewart, R. F.; Pople, J. A. Self-Consistent Molecular-Orbital Methods. I. Use of Gaussian Expansions of Slater-Type Atomic Orbitals. 1969, *51*, 2657–2664.
- [51] Ásgeirsson, V.; Bauer, C. A.; Grimme, S. Quantum chemical calculation of electron ionization mass spectra for general organic and inorganic molecules. *Chem. Sci.* **2017**, *8*, 4879–4895.
- [52] Stepto, R.; Chang, T.; Kratochvíl, P.; Hess, M.; Horie, K.; Sato, T.; Vohlídal, J. Definitions of terms relating to individual macromolecules, macromolecular assemblies, polymer solutions, and amorphous bulk polymers (IUPAC Recommendations 2014). 2015, *87*, 71–120.
- [53] Wang, Y. L.; Saranin, A. A.; Zotov, A. V.; Lai, M. Y.; Chang, H. H. Random and ordered arrays of surface magic clusters. *International Reviews in Physical Chemistry* **2008**, *27*, 317–360.
- [54] Lepeshkin, S. V.; Baturin, V. S.; Uspenskii, Y. A.; Oganov, A. R. Simultaneous prediction of atomic structure and stability of nanoclusters in a wide area of compositions. 2018.
- [55] Lundqvist, M. J.; Nilsing, M.; Persson, P.; Lunell, S. DFT study of bare and dye-sensitized TiO<sub>2</sub> clusters and nanocrystals. 2006, *106*, 3214–3234.
- [56] Nunzi, F.; Agrawal, S.; Selloni, A.; Angelis, F. D. Structural and Electronic Properties of Photoexcited TiO<sub>2</sub> Nanoparticles from First Principles. 2015, *11*, 635–645.